Jada Langston

Elevated Temperatures in the Afar Rift: Perspectives from Carbonate Isotope Geochemistry

submitted in partial fulfillment of the requirements for the degree of

Master of Science in Earth and Environmental Sciences

Department of Earth and Environmental Sciences

The University of Michigan

Accepted by:

Naomi E. Levin	Naomi Levin	8/4/22
Signature	Name	Date
Kyger C Lohmann	Kyger C Lohmann	8/1/22
	Name	Date
Jeroen Ritsema	Jeroen Ritsema	8/4/22
Department Chair Signature	Name	Date

I hereby grant the University of Michigan, its heirs and assigns, the non-exclusive right to reproduce and distribute single copies of my thesis, in whole or in part, in any format. I represent and warrant to the University of Michigan that the thesis is an original work, does not infringe or violate any rights of others, and that I make these grants as the sole owner of the rights to my thesis. I understand that I will not receive royalties for any reproduction of this thesis.

☐ Permission granted.

☑ Permission granted to copy after: <u>12/16/24</u>

☐ Permission declined.

Jada Langston
Author Signature

Earth and Environmental Sciences
UNIVERSITY OF MICHIGAN

Table of Contents

Abstract

The Afar region in Ethiopia is famous both as a location for human origins research and as a volcanically active triple junction. Stable isotopic records from carbonates are some of the primary tools used for studying the paleoecology of early humans under the assumption that they reflect conditions of the initial depositional environment, not subsequent alteration due to burial or hydrothermal activity. However, in the Afar, faulting and volcanism have the potential to alter surface sediments during burial and fluid interactions. These factors are essential for understanding the crustal heat flow in the Afar and the thermal alteration of carbonate deposits. Yet, there are no direct measurements from the rock record that track the variation in thermal gradients in the Afar since the early Pliocene and its effects on carbonate isotopic compositions. Clumped isotope thermometry provides an opportunity to reconstruct carbonate formation temperatures, which gives insight into near-surface crustal heat flow in the Afar during the Pliocene and Pleistocene.

This study sampled carbonates from three settings: 1) carbonates precipitated during or shortly after deposition, 2) post-depositional carbonates formed in voids after sedimentation, and 3) hydrothermal carbonates associated with field evidence of volcanic activity. Stable isotope geochemistry ($\delta^{13}C$, $\delta^{18}O$, and Δ_{47}) of twenty post-depositional and hydrothermal samples was studied in conjunction with an existing isotopic database of 47 carbonates to understand how carbonates record elevated temperatures of the Afar and the effect on carbonate isotopic composition. Characterization of the samples using X-Ray Diffraction and petrography focused on high-temperature carbonates to explore indications of alteration. The range of clumped isotope (Δ_{47}) temperatures (20 – 156 ˚C) from these samples indicates a clear association of higher temperatures (>100 ˚C) from samples <2km with fault and hydrothermal activity, whereas depositional carbonates yield lower temperatures (<40 ˚C), consistent with modern soil temperatures. Post-depositional carbonates show temperatures up to 74 ˚C, typical of Δ_{47} derived temperatures observed in other rifts and overlapping with temperatures observed in thermal (e.g., thermal springs and boreholes) and non-thermal water (lakes, rivers, and shallow wells) in the Afar today. Carbonates directly associated with hydrothermal activity (e.g., calcite dikes, veins) have temperatures between 140 °C and 160 °C, overlapping with the range of Afar geothermal gradients observed in the uppermost crust (<1 km, 36 – 190 ˚C/km). Using the measured Δ_{47}-temperatures and oxygen isotope composition of carbonates ($\delta^{18}O_{carbonate}$), reconstructed $\delta^{18}O$ values of parent waters ($\delta^{18}O_{pw}$) range from -7.7 – +0.5 ‰ (VSMOW) and overlap with water $\delta^{18}O$ values from meteoric waters in the Afar today, which can range from -12 – +2 ‰ (VSMOW). The match between carbonate $\delta^{18}O_{pw}$ values and local meteoric waters is consistent with observations of carbonates in other rift basins or fault systems. These results demonstrate that carbonate isotopic compositions in the Afar can be used as archives of near-surface environmental conditions in depositional settings but are also sensitive to the influence of localized elevated temperatures and hydrothermal activity.

1. Introduction

Stable isotopic records from carbonates have been used extensively to reconstruct the environmental context for human evolution and terrestrial climate records in eastern Africa (Wynn et al., 2000; Levin et al., 2004; Quade et al., 2004; Aronson et al., 2008; Tierney et al., 2017). If the isotopic composition is not altered, stable isotopes can be powerful tools for reconstructing hominin paleoecology (Wynn, 2000; Quade et al., 2004; Aronson et al., 2008; Tierney et al., 2017). However, while the Afar is famous for dozens of Pliocene to Holocene fossil hominins that are critical for human origins research, it is also known for its elevated crustal temperatures as an active triple junction with a mantle plume-induced rift system (Alene et al., 2017; Chorowicz, 2005). The elevated temperatures, extensive faulting, and volcanic activity can affect carbonate preservation in the region, but there has been little to no focus on how these processes influence carbonate records of environmental change in the Afar. Existing studies assume that

most depositional carbonates represent low-temperature surface conditions, without substantial effort to validate these assumptions.

This study investigates whether 1) Afar carbonates in Pliocene and Pleistocene strata record high heat flow and 2) whether elevated temperatures affect isotope-based paleoenvironmental records. This thesis focuses on stable isotope distributions from carbonates that fit into three separate settings: 1) carbonates that formed during or shortly after deposition and reflected surface environmental conditions, 2) post-depositional carbonates that fill voids forming after sedimentation, and 3) carbonates associated with field evidence for volcanic activity.

2. Geological Background

2.1.1. The Afar Region

The Afar region is a triple junction between the African, Somalian, and Arabian plates that separates the Red Sea, Gulf of Aden, and Main Ethiopian rifts, with rifting beginning in the Oligocene and continuing to the present day (Chorowicz, 2005; Alene et al., 2017; Beyene and Abdelsalam, 2005). Most basin-fill sediments accumulated during the Miocene to the Quaternary and are volcanic in origin (e.g., basalts, tufts, ignimbrites) (Alene et al., 2017). These volcanic rocks likely formed as products of a mantle plume during the main phase of volcanism in the Afar, which range from ~30 to ~1 Ma (Alene et al., 2017; Figure 1). The upwelling asthenosphere accounts for the continued continental rifting and the large-scale volcanism in the Afar (Alene et al., 2017). The majority of the non-volcanic sediments are fluvio-lacustrine strata exposed on the western and eastern portions of the Afar.

This study focuses on carbonates from two volcano-sedimentary sections, Gona and Woranso-Mille, in the western Afar that span the Pliocene and Pleistocene (Figure 1). The Gona and Woranso-Mille localities are areas defined by research permits issued to the paleontological and archeological research teams working in these areas over the past 20 years. The primary goals of geologic work in these areas have centered on understanding the chronostratigraphic and environmental context for the fossil and archaeological finds.

2.1.2. Gona Stratigraphy

The Gona locality contains fluvio-lacustrine sediments that document the development of rifting in the western Afar from the late Miocene to the present. Sediments are grouped into four stratigraphic units: Adu-Asa Formation (>6.4 – 5.2 Ma), Sagantole Formation (>4.6 – 3.9 Ma), Hadar Formation (3.8 – 2.9 Ma), and Busidima Formation (2.7 – <0.16 Ma) (Quade et al., 2008; Figure 2). North-South trending normal faults separate the older Adu-Asa and Sagantole Formations and intercalated basalts from the Hadar and Busidima Formation to the east (Figure 1). West of the As Duma Fault, the fluvio-lacustrine sediments of the Adu-Asa and Sagnatole Formations are interbedded with basalts and volcaniclastics, indicating the proximity to volcanic sources. Normal faults dissect the Sagantole Formation, with some sediments showing evidence of hydrothermal alteration (e.g., few vitric tephras preserved). Indications of hydrothermal activity are particularly evident along faults and calcite-filled dikes, including along the As Duma Fault, where multiple small volcanic centers and cinder cones are adjacent to the Sagantole sediments (Quade et al. 2008, Figure 1). East of the As Duma Fault, the basin fill includes the Hadar and Busidima Formations. The Hadar Formation includes lacustrine, fluvial, and deltaic sediments facies, whereas fluvial sediments dominate the Busidima Formation. There is no evidence of hydrothermal alteration, extensive faulting, or local volcanism in either of these units east of the As Duma Fault. There is an extensive record of human evolution throughout these units. The carbonates in these strata have

played an important role in developing the paleoenvironmental context for human evolution. (Semaw et al., 1997; Quade et al., 2004; Semaw et al., 2005; Simpson et al., 2007; Levin et al., 2008; Simpson et al., 2019; Semaw et al. 2020).
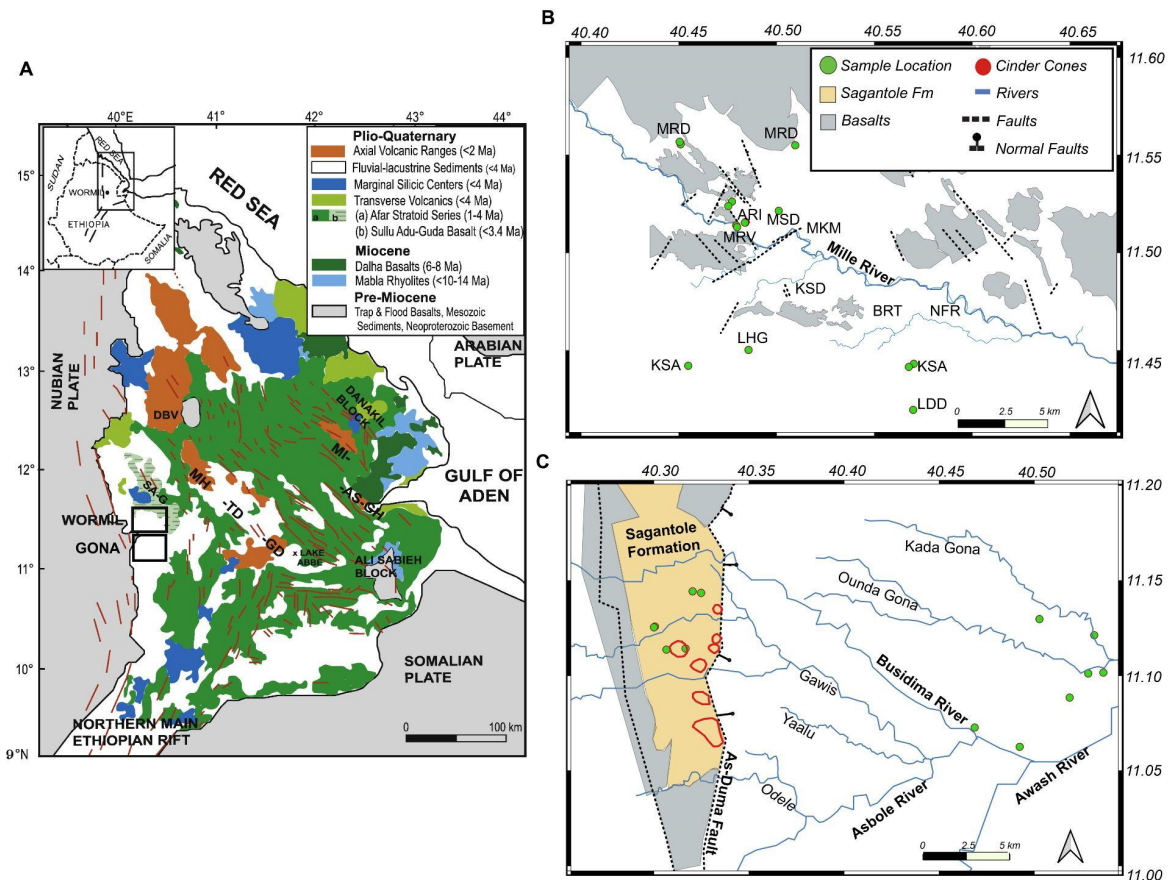

Figure 1: Maps of study locations with A) an overview of the regional geology in the Afar, Ethiopia from Alene et al. (2017), amended with boxes for the locations of the close-up maps for Gona and Woranso-Mille; B) Map of Woranso-Mille with sample locations marked and basalt and fault locations from Alene et al. (2017); C) Map of Gona with sample locations marked and location of basalts, cinder cones, faults. Hadar and Busidima deposits are the white open areas east of the As Duma Fault based on Quade et al. (2008).

2.1.3. Woranso-Mille Stratigraphy

Contrary to the Gona locality, the stratigraphy in the Woranso-Mille region is still under active development. Woranso-Mille is broken into smaller stratigraphic units that correspond to significant fossil hominins found in the area. The stratigraphic sections range from the Pliocene to the early Pleistocene. Fossil collection localities, which have distinct geographic boundaries, define the stratigraphic constraints in this study (Figure 2). The specific relationships of the stratigraphy among these localities are under active study. Overall, the basin-fill of Woranso-Mille is characterized by high sedimentation rates, small normal faults that crosscut sediments, and a large input of local volcanic material. In the strata older than ~3.77 Ma at the LHG and MRD localities (Figure 2), the lacustrine and fluvial sediments are sandwiched between thick, locally derived volcanic units (basalts, ignimbrites). The amount of local volcanic material decreases in units younger than ~ 3.6 Ma (NFR, BRT, LDD). Although there is extensive evidence for the input of local volcanic material (e.g., basalts, ignimbrites) in the Woranso-Mille sedimentary sequence, there is little field evidence of hydrothermal alteration of the fossil-rich lacustrine and fluvial sediments at

Woranso-Mille (Haile-Selassie et al., 2007; Deino et al., 2010; Saylor et al., 2016; Haile-Selassie et al., 2016; Saylor et al., 2019). Like at Gona, the abundant carbonates in Woranso-Mille have provided important contributions to hominin paleoecology (Haile-Selassie et al., 2007; Deino et al., 2010; Saylor et al., 2016; Haile-Selassie et al., 2016; Saylor et al., 2019).

Figure 2: Simplified stratigraphic columns for the sedimentary sequences at Gona and Woranso-Mille. Approximate ages, unit thicknesses, and lithofacies are noted. Formal stratigraphic units are named for Gona but not for Woranso-Mille, where the stratigraphy has not yet been formalized. For Woranso-Mille, fossil localities representing restricted stratigraphic zones are listed instead. Stratigraphic information for Gona is based on Quade et al. (2008), whereas information for Woranso-Mille is compiled from information from Haile-Selassie et al. (2007); Deino et al. (2010); Saylor et al.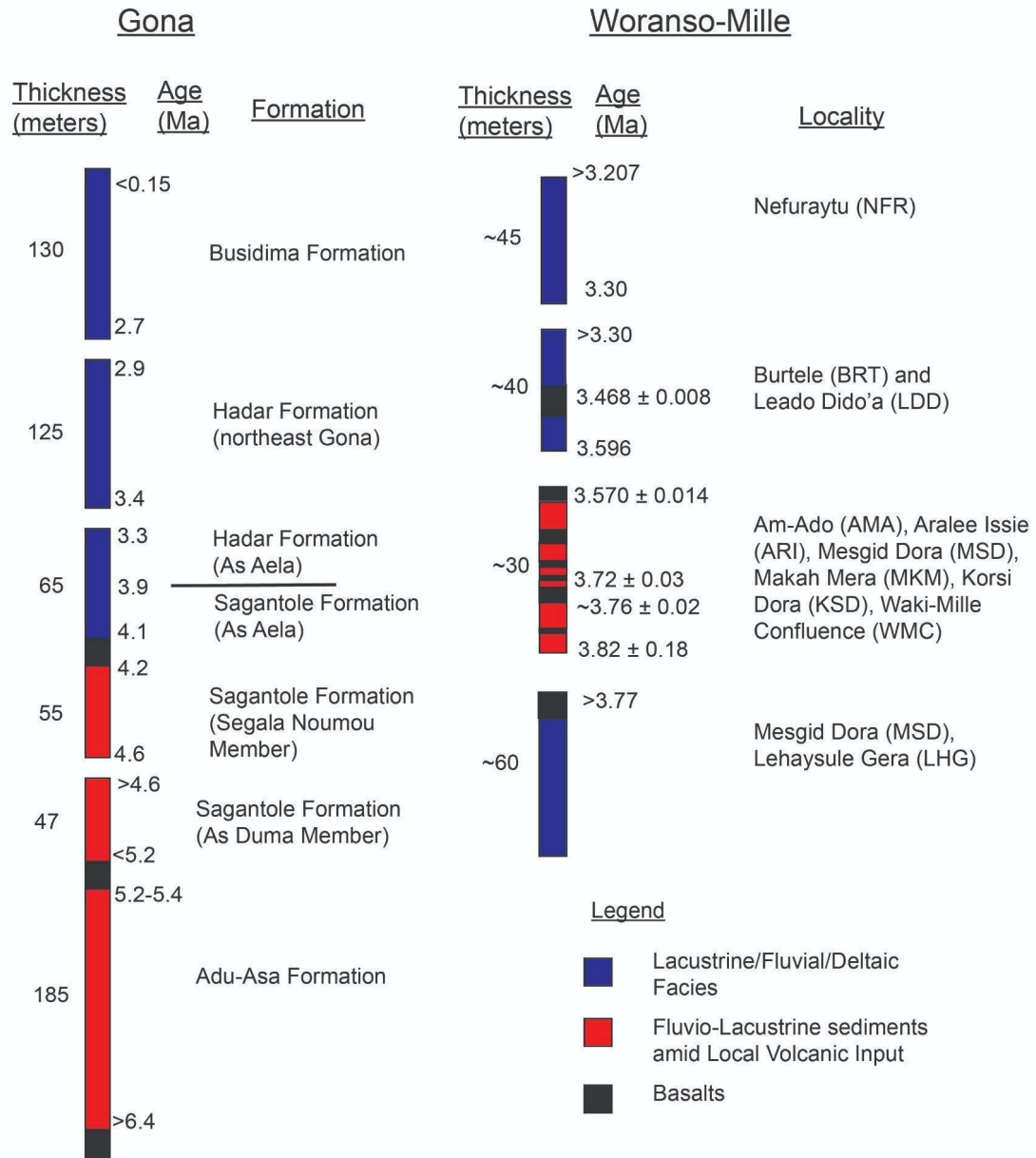 (2016); Haile-Selassie et al. (2016); Saylor et al. (2019). Note that the stratigraphic exposures studied at Woranso-Mille span much less time than those at Gona.

2.2. Heat Flow in the Afar Rift vs. Other Active Rift Settings

Rifting in the Afar sustains the present-day volcanism and high heat flow (Alene et al., 2017; Beyene and Abdelsalam, 2005). Despite the extensive stratigraphic work in the Afar and the importance of carbonate isotope geochemistry in human origins research, no study has systematically tracked the evolution of the heat flow using isotopic archives from rift basin fill. These carbonates could be an untapped resource for tracking past heat and fluid flow in this rift basin.

Table 1. Observed Geothermal Gradients for the Afar and Other Active Rift Systems

Rift System	Gradient * (˚C/km)	Method	Source
Afar	37 – 190	direct temperature measurement*	Bekele, 2012; Zan et al., 1990; Macgregor, 2019
Malawi	25 – 27	aeromagnetic data	Njinju et al., 2019
Jordan	30 – 50	direct temperature measurement*	Myslil, 1988; Sawarieh, 2005
Rio Grande	35 – 40	direct temperature measurement*	Harder et al., 1980
Kenya	15 – 112	direct temperature measurement*; ground magnetic survey	Wheildon et al., 1994; Githiri et al., 2012

* direct temperature measurements from well or drill holes
* data is from the top 1 km from the surface

Borehole measurements well document the high heat flow in the Afar. The geothermal gradient in the Afar ranges from 37 – 190 ˚C/km (for the first kilometer from the surface; Table 1). Geothermal gradients in the Afar vary based on the location but can range from 36 – 190 ˚C/km (Zan et al., 1990, Bekele, 2012; Table 1). Recorded surface water temperatures are ≤100 ˚C, with higher temperatures (60 – 100 ˚C) coinciding with thermal springs or boreholes and lower temperatures coinciding with shallow groundwater, rivers, lakes, and rainfall (20 – 60 ˚C) (Zan et al., 1990; Gizaw., 1996; Houssein et al., 2013; Minissale et al., 2017; Chandrasekharam et al., 2019; Bekele et al., 2021). Deep well and geothermal exploration studies show that at depths larger than 2 km, water temperatures can exceed 200 ˚C (Zan et al., 1990; Gizaw, 1996; Houssein et al., 2013; Minissale et al., 2017; Chandrasekharam et al., 2019; Bekele et al., 2021; Table 2). The Afar geothermal gradient exceeds other active rifts basins, while surface water temperatures are similar. Geothermal gradients from rift systems in Malawi, Kenya, Jordan, and the Rio Grande vary from 23 – 40 ˚C/km, with some estimates that the Kenyan Rift Basin varies between ~69 – 111 ˚C/km (Githiri et al., 2012; Table 1). Surface water temperatures from the Jordan, Kenya Rift, and Rio Grande Rift all fall below 100 ˚C, similar to the Afar (Blomgren et al., 2019; Sass et

al., 2014; Renaut et al., 2013; Renaut et al., 2002; Table 1 and 2). Assuming similar thermal conductivities and based on known geothermal gradients, the Afar rift system seems to have a higher heat flow than other active rifts. This thesis evaluates whether it is possible to detect the high heat of the Afar within carbonates using clumped isotope thermometry, a thermodynamically based approach for reconstructing carbonate formation temperatures.

Table 2. Published Water Temperatures from Active Rift Systems

Rift Setting	Water Type	Temperature (°C)	Source
Afar	Thermal Springs and Pools; Drilled Boreholes; Fumaroles	23 – 98	Zan et al., 1990; Houssein et al., 2013; Minissale et al., 2017; Chandrasekharam et al., 2019; Bekele et al., 2021
Afar	Lakes, Thermal Springs, Groundwater, etc.	20 – 98	Gizaw, 1996
Rio Grande	Thermal Springs, Meteoric Waters, Wells	15 – 88	Blomgren et al., 2019
Jordan	Thermal Springs	20 – 62	Sass et al., 2014
Kenya	Hot Springs	28 – 98	Renaut et al., 2002; Renaut et al., 2013
Kenya	Lake Water	23 – 27	Renaut et al., 2002

2.3. Clumped Isotope Thermometry

Carbon and oxygen isotopes of carbonates are well-established tools for reconstructing paleoecology and paleoclimate in eastern Africa during the Pliocene to Pleistocene (Cerling, 1992; Wynn, 2000; Levin et al., 2004; Quade et al., 2004; Aronson et al., 2008). Notation of carbon and oxygen isotopes is represented with the delta symbol (δ), which is calculated using the R or the ratio of the abundance of the heavy, rare (^{13}C and ^{18}O) to light, abundant (^{12}C and ^{16}O) isotopes between the sample and the standard.

$$\delta = (\frac{R_{sample}}{R_{standard}} - 1) \times 1000 \text{ Eq (1)}$$

However, $\delta^{18}O$ values of the carbonate ($\delta^{18}O_{carbonate}$) can be challenging to interpret because both the carbonate formation temperature and the oxygen isotopic composition of its parent water ($\delta^{18}O_{pw}$) influence the $\delta^{18}O_{carbonate}$. Clumped isotope thermometry is an isotope technique gaining traction over the past decade because it reconstructs carbonate formation temperatures and, with $\delta^{18}O_{carbonate}$, reconstructs $\delta^{18}O_{pw}$ values (Ghosh et al., 2006; Eiler, 2007). Clumped isotopes are isotopologues containing two or more rare isotopes (in this case, ^{13}C and ^{18}O) that preferentially "clump" together in a molecule as a

function of temperature (Schauble et al., 2006; Ghosh et al., 2006; Eiler, 2007; Mangenot et al., 2017). Clumped isotope thermometry measures the abundance of molecules with the mass 47 isotopologues (specifically $^{13}C^{18}O^{16}O$) from CO_2 released after acid digestion in a sample and compares it to the expected stochastic distribution mass 47 based on the abundance of ^{13}C and ^{18}O in the sample. Δ_{47} represents the relative abundance of mass 47, a ratio between the mass 47 in the CO_2 molecule relative to the stochastic distribution of isotopologues in units per mil (‰) (Eiler, 2007).

$$\Delta_{47} = \left[\frac{R^{47}}{2R^{13}*R^{18}+2R^{17}*R^{18}+R^{13}*(R^{17})^2} - \frac{R^{46}}{2R^{18}+2R^{13}*(R^{17})^2} - \frac{R^{45}}{R^{13}+2R^{17}} + 1 \right] * 1000 \quad \text{Eq (2)}$$

R is the ratio of the most abundant isotopologue to the minor isotopologue of the CO_2 molecule (i.e., $R^{13} = {}^{13}C/^{12}C$; $R^{18} = {}^{18}O/^{16}O$; $R^{47} = {}^{13}C^{18}O^{16}O /^{12}C^{16}O^{16}O$). The carbonate Δ_{47}-temperature relationship has been calibrated in laboratories for inorganic and biogenic carbonates for temperatures between 0 – 350 ˚C in a range of conditions (e.g., pH, different mineralogy, salinity) and matches theoretical conditions (Ghosh et al., 2006; Henkes et al., 2013; Bonifacie et al., 2017; Kele et al., 2015; Kelson et al., 2017; Mangenot et al., 2017). The laboratory experiments confirm that carbonate Δ_{47} values can accurately reconstruct the temperature during precipitation for a variety of carbonate types (Ghosh et al., 2006; Henkes et al., 2013; Bonifacie et al., 2017; Kele et al., 2015; Kelson et al., 2017; Mangenot et al., 2017). By combining the reconstructed carbonate Δ_{47}-temperatures and $\delta^{18}O_{carbonate}$ values, it is possible to reconstruct the $\delta^{18}O$ values of the parent waters ($\delta^{18}O_{pw}$) during carbonate formation or the $\delta^{18}O$ values of the diagenetic fluids that altered the carbonate (Ghosh et al., 2006; Eiler, 2007). In addition, recent studies show the potential for using clumped isotope thermometry to explore kinetic effects related to burial, resetting, and solid-state reordering of C-O bonds, which is not possible with measurements of $\delta^{18}O_{carbonate}$ alone (Henkes et al., 2014; Shenton et al., 2015; Chen et al., 2019). With the high heat flow in the Afar (Section 2.2), there is great potential to use carbonate clumped isotope thermometry to explore elevated temperature effects on the sediments preserved in its rift basins.

2.4. Carbonate Δ_{47}-temperatures and $\delta^{18}O_{pw}$ reconstructions in Rift Systems and Fault Zones

In the past decade, advances in clumped isotope thermometry have changed the interpretations of isotopic records of soil carbonates (e.g., Passey et al., 2010; Quade et al., 2013; Kelson et al., al., 2020). In eastern Africa, several studies on carbonates that span the Pliocene to modern demonstrate the value of this new approach (e.g., Passey et al., 2010, Quade et al., 2013; Ludecke et al., 2018; Beverly et al., 2021). Pliocene and Pleistocene carbonate Δ_{47}-temperature records from the Omo-Turkana Basin of Kenya and Ethiopia and the Karonga Basin in Malawi yield temperatures that range from ~20 – 40 ˚C (Passey et al., 2010; Ludecke et al., 2018), similar to modern soil temperatures measured in the Afar, Turkana, and the Serengeti region of Tanzania (Passey et al., 2010; Ludecke et al., 2018; Beverly et al., 2021). Among modern soil carbonate Δ_{47}-temperature from eastern Africa (Passey et al., 2010; Beverly et al., 2021) and those analyzed from elsewhere in the world (Kelson et al., 2020), Δ_{47}-temperatures from soil carbonates today rarely exceed 40 ˚C. This thesis will treat depositional carbonates that yield temperatures exceeding 40 ˚C cautiously, even though temperatures >40 ˚C do not necessarily imply alteration.

Many Δ_{47}-temperature studies focus on low-temperature carbonates for paleoclimate reconstructions. Recent high-temperature (>100 ˚C) carbonate Δ_{47}-temperature calibrations (Bonifacie et al., 2017; Peterson et al., 2019) enable carbonate clumped isotope thermometry to probe tectonic, diagenetic, and metamorphic processes (e.g., Lacroix and Niemi, 2019; Brenner et al. 2021; Brigaud et al. 2020). Considering the potential use of clumped isotope thermometry to study the temperature history in the Afar, it is useful to understand the existing clumped isotope studies on carbonates associated with elevated heat sources in other rift systems. Δ_{47} carbonate temperatures values from vein calcites and diagenetic carbonates from other rifts (Moab Fault, Mormon Peak detachment, Paris Basin, South Pyrenean Frontal Thrust, San Andreas Fault) range from 7 – 134 ˚C (Swanson et al., 2012; Bergman et

al., 2013; Hudson et al., 2016; Luetkemeyer et al., 2016; Brigaud et al., 2020; Hoareau et al., 2021) (Table 3). With the Afar possessing a higher heat flow relative to other rifts, carbonates influenced by hydrothermal activity or post-depositional processes should match or exceed the Δ_{47}-temperatures observed in other rift systems.

While using Δ_{47}-temperatures to explore the influence of elevated temperatures on Afar carbonates preserved in sedimentary basins, these temperatures can also provide constraints for reconstructing the oxygen isotopic compositions of parent waters ($\delta^{18}O_{pw}$). Variations in $\delta^{18}O_{pw}$ values can help assess the origins of the fluids from which carbonates formed. In other studied rift systems for which there are Δ_{47}-temperature data, reconstructed $\delta^{18}O_{pw}$ values matched local meteoric waters or were a mixture of meteoric or marine water with deeper fault fluids (Swanson et al., 2012; Bergman et al., 2013; Hudson et al., 2016; Luetkemeyer et al., 2016; Brigaud et al., 2020; Hoareau et al., 2021).

Table 3. Published carbonate Δ_{47}-temperature values in other rift or fault settings

Rift/Fault Setting	Carb Type	Age Approximate	Temperatures (°C)	Source
Moab Fault, Utah	Vein calcites	Permian and mid-Tertiary	$7 - 73$	Hodson et al., 2016
Mormon Peak Detachment	Cataclastic rocks, narrow vein fillings, and larger void-filling carbonates	Miocene	$24 - 137$	Swanson et al., 2012
Paris Basin	Diagenetic calcite cements	Eocene and Oligocene	$30 - 109$	Brigaud et al., 2020
South Pyrenean Frontal Thrust (Spain)	Tectonic calcite veins	Late Cretaceous to the Early Miocene	<90	Hoareau et al., 2021
Moab Fault, Utah	Calcite cements fault intersection hosts cements	Permian and mid-Tertiary	$13 - 128$	Bergman et al., 2013
San Andreas Fault	Vein calcites	Not included	$81 - 134$	Luetkemeyer et al., 2016

To use $\delta^{18}O_{pw}$ values for evaluating depositional and diagenetic information preserved in carbonates from the Afar, it is essential to understand the ranges in $\delta^{18}O$ values of different types of waters from the Afar. Published $\delta^{18}O$ values from waters in the Afar vary between -12 – +10.3 ‰. Mean amounted-weighted precipitation $\delta^{18}O$ values range from -2.1 – -1.3‰ for stations in the highlands of Ethiopia, although daily precipitation $\delta^{18}O$ values can vary from -12.6 – +10.3 ‰. Long-term precipitation datasets are unavailable for the Afar, but the $\delta^{18}O$ values of non-thermal surface waters and groundwater range from -3 – +5 ‰. In comparison, thermal springs and boreholes have low $\delta^{18}O$ values (-8 – -5 ‰) (Levin et al., 2009; Alemayehu et al., 2017; Bedaso et al., 2020; Kebede et al., 2021). For comparison to Afar carbonate reconstructed $\delta^{18}O_{pw}$ values, this thesis bins Afar water $\delta^{18}O$ values into three groupings: thermal springs and high-temperature boreholes, non-thermal surface waters, boreholes, and springs (lakes, rivers, springs, wells, etc.), and precipitation (Levin et al., 2009; Alemayehu et al., 2017; Bedaso et al., 2020; Kebede et al., 2021). Comparing the isotopic data from these three categories to reconstructed $\delta^{18}O_{pw}$ explores whether there are distinctions in $\delta^{18}O_{pw}$ values among the different carbonate types that might provide additional insight into their formation.

3. Methods

3.1. Sample Collection

Carbonate samples were collected during fieldwork conducted as part of the paleoanthropological research in the Gona and Woranso-Mille areas. Gona samples were collected between 1999 to 2007, while Woranso-Mille samples were collected in 2011 and 2018. Carbonate collections focused on pedogenic carbonates for paleoenvironmental reconstruction, but other carbonate types were collected opportunistically during fieldwork as they were encountered. The carbon and oxygen isotopic composition of pedogenic carbonates has been published in many publications (e.g., Levin et al. 2004; Haile-Selassie et al. 2012; Haile-Selassie et al. 2016; Levin et al. 2022). Bedaso et al. (in prep) selected a subset of these samples (n = 47) for Δ_{47} analyses, focusing on pedogenic carbonates, to evaluate environmental temperature change through the sequence. This research builds on and expands this dataset to include Δ_{47} analyses of 20 additional carbonate samples with petrographic analysis (n = 21) and X-Ray Diffraction (n = 5) to evaluate carbonate paragenesis, specifically focusing on samples that represented different morphologies and near hydrothermal, fault, and volcanic activity. This project focuses on samples that investigate how Afar carbonates record heat flow and determine its influence on the stable isotopic composition of depositional carbonates. This research was restricted to laboratory analysis of previously collected samples as additional fieldwork was not possible.

Samples were grouped into three overarching categories (Table 4) based on their field context and initial morphological descriptions from hand samples: depositional carbonates, post-depositional, and hydrothermal carbonates. Depositional carbonates are associated with sedimentary facies and formed during or shortly after deposition (Figure 3), post-depositional carbonates are void infills that formed after sedimentation (Figure 8), and hydrothermal carbonates are associated with field observations of volcanic activity (Figure 9). These samples were further characterized by thin section and XRD analysis based on their proximity to hydrothermal sources and isotopic compositions. Based on the morphological descriptions and petrographic analysis, this project further subdivides carbonates into more specific categories within the three overarching categories (Table 4).

3.2. Petrography

Twenty-one carbonate samples were sent to Spectrum Petrographic to be double polished, cut to 30 microns, and placed on a glass plate for basic petrographic analysis under a Zeiss microscope scope at the University of Colorado-Boulder.

3.3. X-Ray Diffraction (XRD)

Five carbonates of different morphologies were selected to determine the bulk mineralogy of the carbonates of samples that were either close to heat sources or because of their distinct morphology. These samples included three concretions (two outer rim samples and one core sample), the fault carbonate sample from Woranso-Mille, and hydrothermal carbonate samples from the Sagantole Fm at Gona. The samples were crushed, and 50 mg of powder was analyzed using the Rigaku Ultima IV Diffractometer at the University of Michigan Electron Microbeam Analysis Lab (EMAL).

Table 4. Carbonate categories used for the study.

Broad Carbonate Categories	Specific Carbonate Types
Depositional	Concretions
	Carbonate Ledge
	Marls
	Pedogenic Nodules
Post-Depositional	Fault Calcite
	Basalt Calcite
	Gravel Cement
	Bone Calcite
	Mollusc Spar
Hydrothermal	Dike Calcites

3.4. Clumped Isotope Thermometry

Carbonates were analyzed at John Hopkins University (JHU) and the University of Michigan (UM) Isotopologue Paleosciences Lab for carbonate Δ_{47}, $\delta^{18}O$, and $\delta^{13}C$ values. The data from JHU are included in Bedaso et al. (in prep) as part of a study focusing on pedogenic carbonates, with all data from UM being new in this thesis. The analytical methods between the labs are very similar and sometimes use the same equipment. All carbonate samples were first powdered using a rotary Dremel tool or a mortar and pestle, and 8 – 10 mg of sample powder were used for each analysis. In both labs, $\delta^{13}C$, $\delta^{18}O$, and Δ_{47} analyses of carbonates were accomplished using a custom build device, as described in Passey et al. (2010), that reacts carbonates in a common acid bath of 100 % H_3PO_4 at 90 ˚C and purifies the resultant CO_2 in a series of cryogenic traps including a Gas Chromatograph (GC) column at -20 °C. Purified CO_2 gas was then transferred to the dual inlet system of the mass spectrometer. Samples were analyzed on a Thermo Scientific MAT 253 isotope ratio mass spectrometer (IRMS) at JHU and a Nu Perspective IRMS at UM.

Clumped isotope data from both labs were analyzed with respect to an absolute reference frame or the 'carbon dioxide equilibrium scale' (CDES), which empirically corrects for instrumental nonlinearities and changes in the ionization from the mass spectrometer (Dennis et al., 2011). The CDES reference frame for processing raw Δ_{47} values consists of international clumped carbonate reference standards, depleted and enriched gasses equilibrated at 30 °C, and those heated at 1000 °C distributed between the samples in all runs. At JHU, carbonate reference materials included NBS-19 and two internal carbonate standards, UU-Carrara, and 102-GC-AZ01. At UM, they also included the carbonate reference materials used at JHU and the more recently developed standards ETH1, ETH2, ETH3, and ETH4. At JHU, all equilibrated gas reference materials were prepared off-line and introduced into the mass spectrometer with a tube cracker. At UM, an online device was used to introduce these reference gasses.

For analyses from both labs, raw Δ_{47} data were corrected to standards using a fixed slope fitted to the carbonate standards and isotopologue equilibrated gas at 1000 °C and 30 °C. All Δ_{47} values reported in this paper use the CDES90 reference frame with an acid correction factor of 0.082 ‰ to adjust to the 25 °C acid digestion frame (Passey et al., 2010; Defliese et al., 2015). All data are reported in Table 5. Note that the Δ_{47} data reported here have not been corrected using the methods outlined by Petersen et al. (2019) to account for [17]O corrections and interlaboratory calibration work.

The Δ_{47} isotopic values were converted into temperature values using the calibration equation for carbonates with temperatures in Kelvin from -1 – 300 °C from Bonifacie et al. (2017):

$$\Delta_{47CDES90} = 42200/T^2 + 0.1262 \text{ (Eq 3) for a 90 °C acid digestion reference frame}$$

Reconstructed $\delta^{18}O_{pw}$ values were calculated from $\delta^{18}O_{carbonate}$ values and Δ_{47} derived temperatures, assuming equilibrium fractionation during the formation of calcite from water, following the equation for equilibrium fractionation from Kim and O'Neil (1997), where T is the temperature in Kelvin:

$$1000ln\alpha_{calcite-H2O} = (18.03 \times 10^3/T) - 32.42 \text{ Eq (4)}$$

and $\alpha_{calciteH2O}$ is the fractionation factor for calcite formed in equilibrium with water which can be used to reconstruct the $\delta^{18}O$ value of the parent water ($\delta^{18}O_{pw}$).

$$\alpha_{calcite-H2O} = \frac{(1000+\delta^{18}Ocalcite)}{(1000+\delta^{18}Owater)} \text{ Eq (5)}$$

3.5. Error

Average Δ_{47}, $\delta^{18}O$, and $\delta^{13}C$ values are reported on the replicate analyses (n = 2–4) for each sample. The standard deviation (1σ) for the majority of replicate Δ_{47} analyses is 0.03‰ (Table 5). Error on temperature estimates and reconstructed $\delta^{18}O_{pw}$ values are reported as 1σ from replicate analyses, but the actual error must be propagated to account for error in Equation 2. This will be done when the study is prepared for publication.

4. Results

4.1. Petrography and Carbonate Descriptions

This section reports descriptions of the carbonates analyzed for clumped isotope data (n = 67). These samples are categorized using a combination of field observations from their geologic context, hand sample descriptions, and thin section petrography (see Table 4 for categories). These categories are provisional ways to group the samples. The X-Ray Diffraction (XRD) results are from the five chosen samples to investigate mineralogy in relation to elevated temperatures (e.g., dike calcites, concretions). The XRD data from these samples indicate that the dominant carbonate mineralogy is calcite (Supplemental Figures 1 – 4), with trace amounts of lanarkite, erniggliite, or $T_{l2}SnAs_2S_6$. XRD data from all five samples analyzed indicate similar distributions of minerals. Additional XRD work on samples is needed, but initial examination of samples in thin-section confirms calcite as the dominant mineral in samples. XRD data are reported in the supplemental material.

4.1.1. Depositional Carbonates

Depositional carbonates are associated with sedimentary facies and represent conditions during or very soon after sedimentation, before the burial of a unit (Figure 3). These carbonates have no direct association with hydrothermal or fault activity and are the primary carbonates used for paleoecological reconstructions in the Afar.
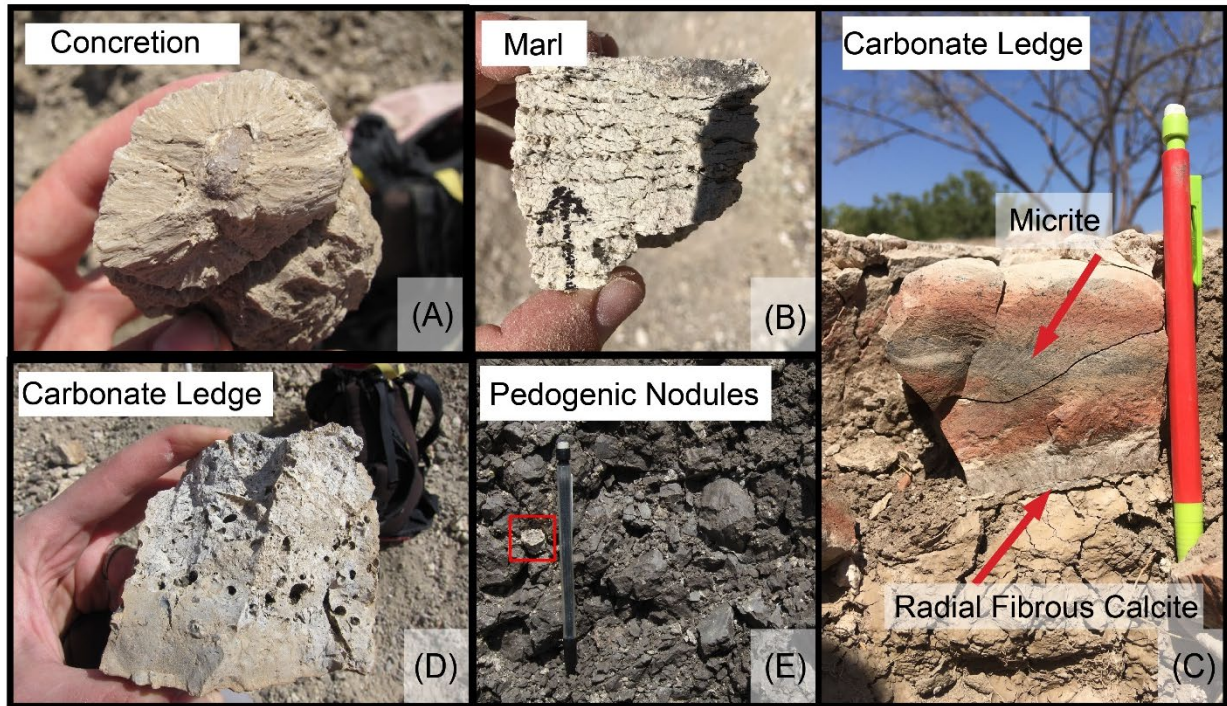

Figure 3: Representative field photos of depositional carbonates in the Afar. A) Radial concretion with a core, B) Marl with clear bedding. C) The carbonate ledge, WM18-KSA-275X, has two distinct portions (micrite and radial fibrous calcite) studied for isotopic analysis. D) A mollusc-bed carbonate ledge with the voids that are mollusc molds. E) Pedogenic nodules in a paleosol, with nodules outlined in the red rectangle. Hand for scale in A, B, and D and pencil for scale in C and D.

Pedogenic Nodules (n=38)

Pedogenic carbonate nodules are in the Bk horizon of paleosols sampled from Woranso-Mille and Gona. Nodules are associated with pedogenic features, such as ped structures, clay cutans, or slickensides on ped faces. Samples are collected at least 30 cm below the surface to avoid the influence of atmospheric CO_2 and near-surface evaporation on the $\delta^{13}C$ and $\delta^{18}O$ values of pedogenic carbonate nodules. These carbonates are sub-angular and nodular shaped, ranging from 1 – 5 cm in width, white to gray, and mostly micrite with clay from surrounding sediment within the matrix (Figure 3E). Preliminary petrographic work on nodules from the Sagantole Fm indicates recrystallization of the nodules and cement filling intranodular voids of the carbonate matrix (Figures 4B, C). Preliminary petrographic work on a pedogenic nodule from the Hadar Fm shows no alteration (Figure 4A), while a nodule from Woranso Mille shows the presence of spar on its edges (Figure 4D).

Marls (n=10)

At Woranso-Mille, marls are prevalent in stratigraphic sections in the LHG, MRV, and MRD fossil collecting areas. Marls are micritic carbonates associated with lacustrine facies. They are 1 – 4 cm thick horizons, with well-sorted silt to clay size grains, and often have black or orange staining (Figure 3B). They are primarily brown or gray micrite in thin sections, with some holes and cracks filled with spar (Figure 5). Thin sections of samples WM18-MRD-231X, WM18-LHG-252, and WM18-LHG-253 show

quartz veins or crystals intertwined with the micrite (Figure 5A), which may indicate possible silicification of the carbonate from precipitation of quartz. One marl has radial fibrous calcite on the edges, similar to structures observed in the radial concretions and in the WM18-KSA-275X carbonate ledge (Figure 5D).
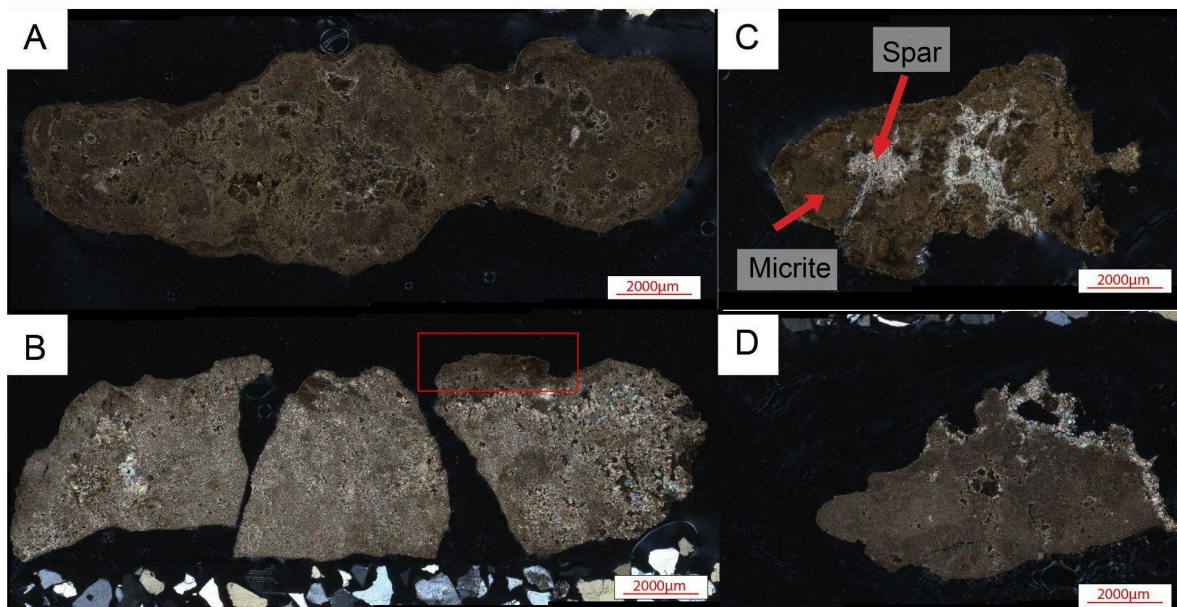

Figure 4: Representative cross-polarized light images of pedogenic nodules. A) The nodule GONJQ-036A (Hadar Fm) is composed of fine to coarse-grained micrite (the brown material) with some zones of spar. B) GONJQ-242 (Sagantole Fm) is almost completely recrystallized material with a few pieces of brown micrite on the edges of the carbonate, as indicated by the red box. C) GONNL-038 (Sagantole Fm) is mostly fine-grained micrite with large spar inclusions in the nodule. D) WM11-ARI-125 (Woranso-Mille) is dominated by fine to coarse-grained micrite with spar lining some edges of the nodule.

Radial Concretions (n=3)

In this study, the term radial concretion refers to near spherical gray radial fibrous carbonates ranging from 4 – 7 cm in diameter, and they appear to be denser than the other carbonate types (Figure 3A). These concretions outcrop in Woranso-Mille and Gona along bedding and association with lacustrine and deltaic facies; however, more fieldwork is needed to understand their distribution. Some concretions have a black circular inner core (2 cm diameter) with a crystalline rim of radial fibrous carbonate surrounding it (e.g., WM11-KSA-162), whereas other concretions have no core (e.g., WM11-LDD-142 and GONJQ-294). XRD data from WM11-KSA-162 and WM11-LDD-142 samples indicate that the crystalline rim is calcite with a secondary mineral (possibly barite or lanarkite, erniggliite, $Tl_2SnAs_2S_6$) that may be the reason for the high density (Supplemental Figures 2 – 3). From thin section analysis, these radial fibers are homogenous across the sample and are crystalline calcite (Figures 6A – B). Radial concretions are initially among the depositional carbonates because we hypothesize that these are associated with depositional processes; however, this grouping and interpretation is temporary as we learn more about the conditions in which they formed.
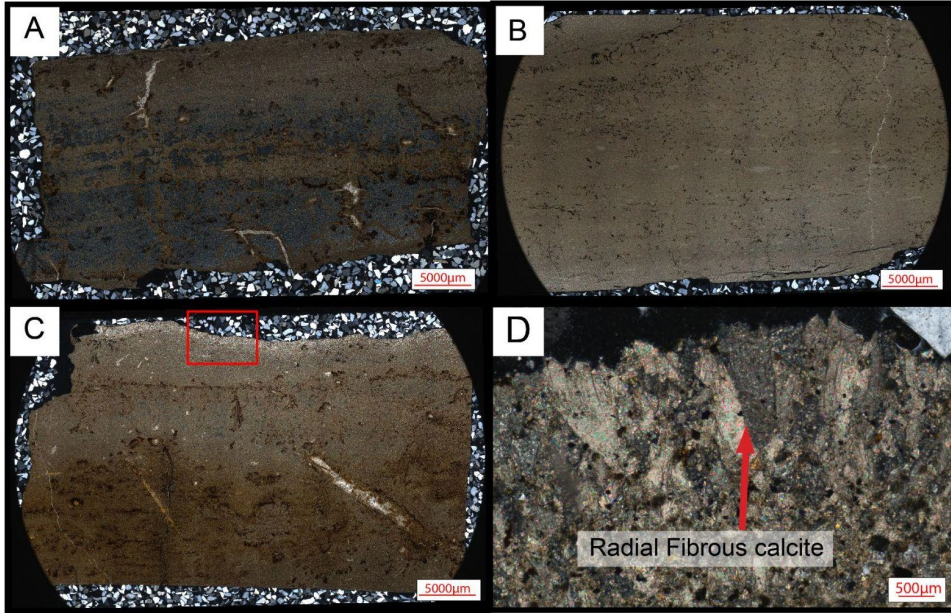
Figure 5: Representative cross-polarized light images of marls. A) WM18-MRD-231X is comprised of micrite (the brown material), quartz likely from silicification of the marl, and filled voids. B) WM18-MRD-217X is composed of only micrite, which is representative of most of the marl samples studied for this thesis. C) WM18-MRD-232X is majority micrite with some spar inclusions. The red rectangle represents the area of the section represented by the close-up image in photo D. D) A zoomed-in portion of WM18-MRD-232X where the edge has radial fibrous textures.
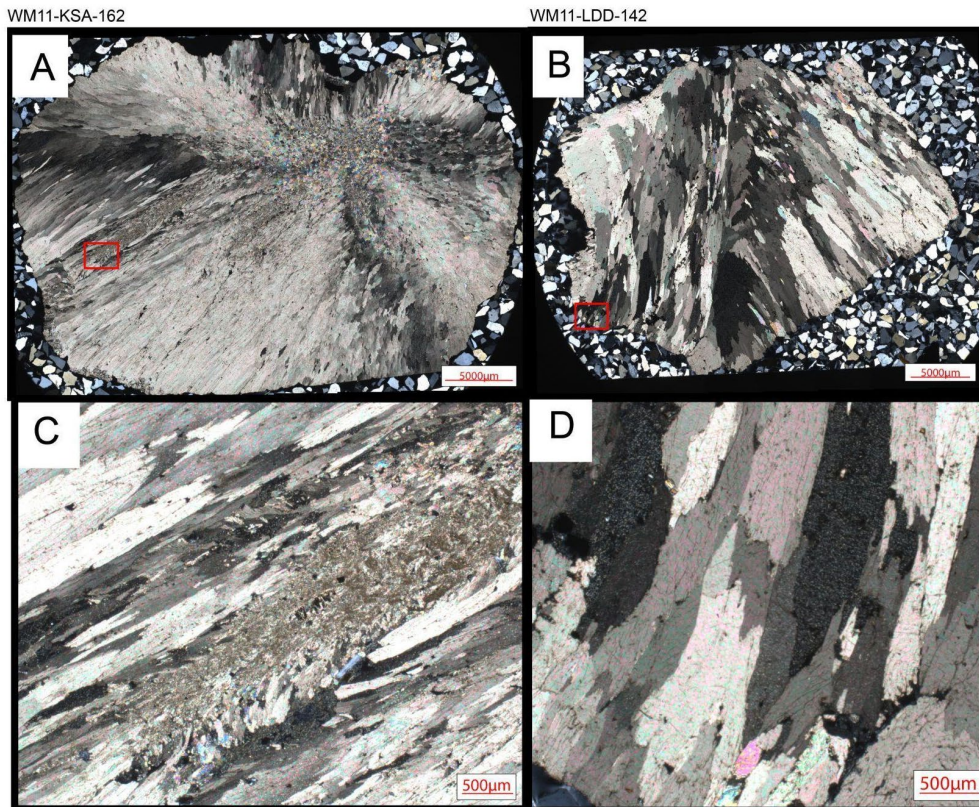

Figure 6: Representative cross-polarized light images of radial concretions. A) WM11-KSA-162 contains radial fibrous calcite that has nucleated around a core, where the red rectangle represents the area magnified in panel C. B) WM11-LDD-142 is similar to WM11-KSA-162 but contains larger and coarser fibers; the red rectangle represents the area magnified in panel D. C) Close-up of WM11-KSA-162 depicting the fine radial fibrous calcite of the concretion and showing spar infill that has precipitated between the radial fibers. D) Close-up photo showing the radial calcite fibers in WM11-LDD-142.

16

Carbonate Ledge (n=3)

Carbonate ledges are indurated micritic carbonate units, 2 – 10 cm thick and laterally continuous, and are common within the fluvio-lacustrine strata at Gona and Woranso-Mille (Figures 3C –D). There are two types of carbonate ledges found. One type of carbonate ledge (WM18-KSA-275X; Figure 3C) is from the fluvial facies at the KSA fossil site at Woranso-Mille has two distinct parts: the top portion, which is micritic, and typical of carbonate ledges (WM18-KSA-275XA) and the basal unit of fibrous calcite (WM18-KSA-275XB). The top micritic ledge is a 2 – 4 cm reddish-brown silty carbonate with indications of desiccation cracks and black dendrites visible from the top of the unit. The base is a 1 – 2 cm whitish-gray carbonate with fibers oriented perpendicular bedding which, under thin section, resemble the radial fibers found in the one marl sample and radial concretion (Figures 5D, 6A – B, 7C – F). Thin sections of the upper micritic portion show that the reddish-brown material is micrite with voids filled with calcite spar (Figure 7E). The second type of carbonate ledge is micritic with extensive molluscan molds from the ARI area at Woranso-Mille, where no original mollusc material remains (Figure 3D).
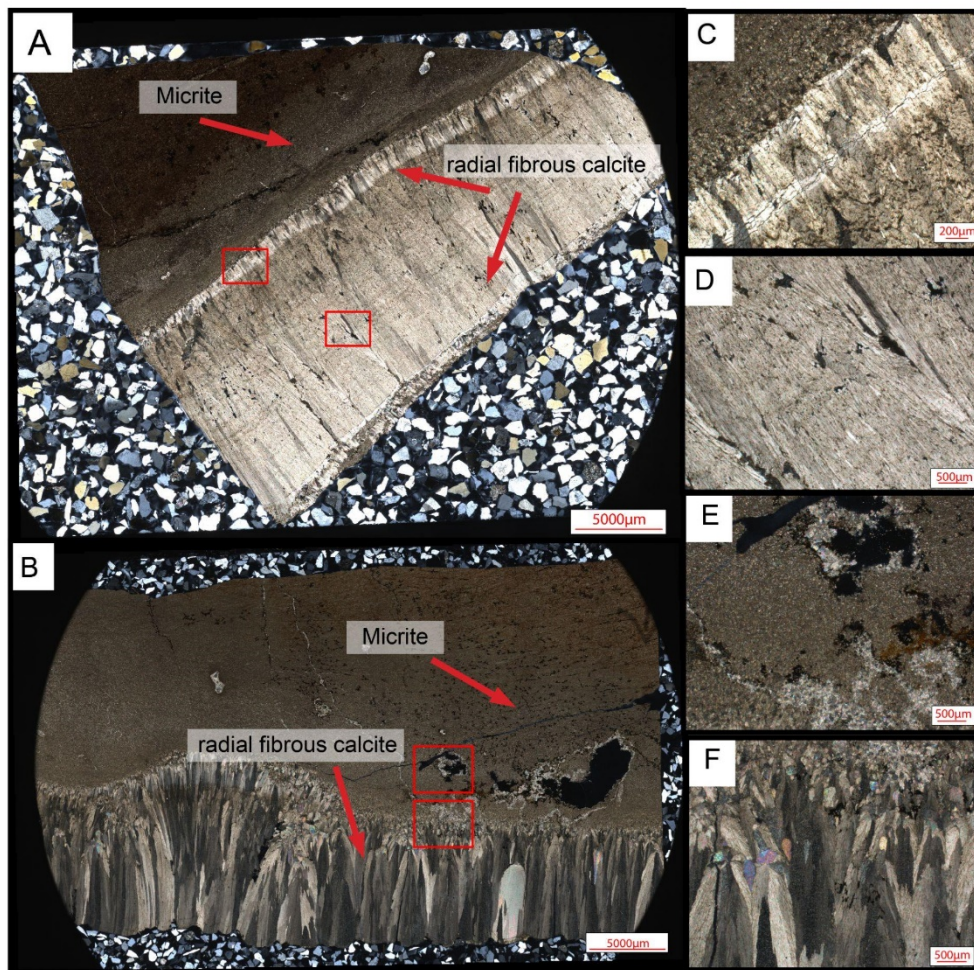

Figure 7: Representative cross-polarized light images of a carbonate ledge sample. WM18-KSA-275X. A) Mosaic photo of WM18-KSA-275X. This carbonate is mainly composed of two materials 1) brown micrite material and 2) radial fibrous calcite. The ledge has three distinct layers, with the micrite in the first layer and the radial fibrous calcite being the other two. The red rectangle represents the section where photos C and D are found. B) Another mosaic photo of WM18-KSA-275X showing the micrite and radial fibrous calcite portions, where the radial calcite is coarser and thicker than in panel A, with some inclusions of the spar in the micrite. The red rectangle represents the section where photos E and F are found. C) Zoomed in portion showing the boundary between the micrite and the radial fibrous calcite fibers. D) The very fine fibers of the radial fibrous calcite. E) Micrite material with spar filling voids. F) Thick and coarse radial fibrous calcite material.

4.1.2. Post-depositional Carbonates

Post-depositional carbonates (n=11) represent a broad category of carbonates in voids with clear indications that they formed after sedimentation (Figure 8). These voids include vesicles of basalts intercalated with sediment, interstitial space of conglomerates, in the intraskeletal cavities of fossil mammal bones, spar and micrite associated with mollusc beds, and along faults. Due to the size and instability of the carbonates, no post-depositional carbonate thin sections exist, and because of the broadness of this category, the samples are broken into five subcategories:
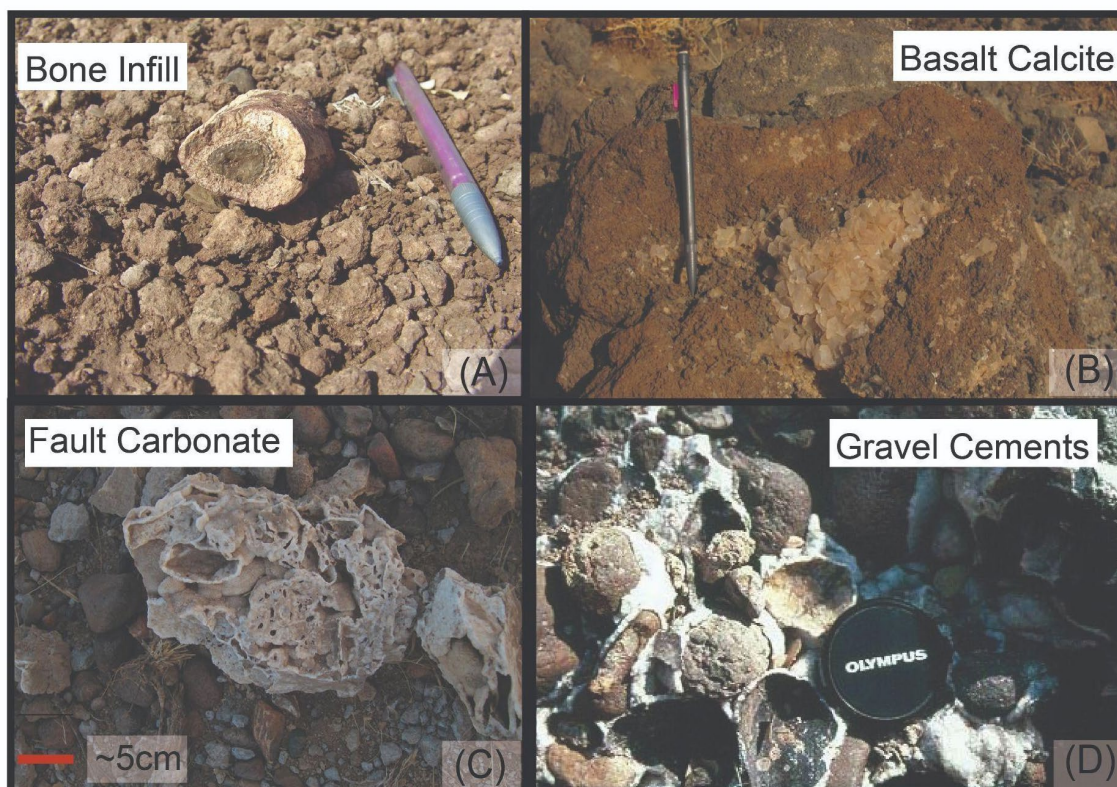

Figure 8: Representative field photos of post-depositional carbonates in the Afar. A) Bone infill calcite with the pencil for reference. B) Basalt calcite infill. C) Fault carbonate that formed in cross-cutting fault sediments in Woranso-Mille. D) Example of gravel cement. Note that the cement is infilling the voids around the pebbles and cobbles. A pencil is used for scale in A and B, and a camera lens cap is used for scale in D.

Basalt Calcites (n=1):

The basalt calcite is a single sample with anhedral and euhedral calcite crystals that fill the vesicles within basalt intercalated with sediments in the ARI stratigraphic sections of Woranso-Mille (WM11-ARI-135; Figure 8B). These crystals are between 1 – 3 cm in length.

Gravel Cement (n=1):

Gravel cements are sparry calcite cement formed in the interstitial space around pebbles and cobbles in fluvial channels. Gravel cements are abundant at Gona; the single sample examined in this study is from the Busidima Fm (GONJQ-103; Figure 4D).

Bone Infill (n=4):

This category includes calcites formed in the cavities of fossil mammal bones from the Sagantole Fm at Gona (Figure 8A).

Spar Infills (n=3):

These carbonates are from spar-filled cracks, sparry fossil casts associated with mollusc beds, and small compact mud concretions from the Sagantole Fm and Woranso-Mille.

Fault Carbonate (n=1):

The fault carbonate is a single sample of septarian calcite with spar forming along with small NW-SE trending faults in the MSD area of Woranso-Mille (WM11-MSD-102). Unlike the dike calcites (see Section 4.1.3), these carbonates are not associated with indications of hydrothermal activity (such as the orange staining around the vein) and do not include large euhedral calcite crystals. XRD data indicates that the fault carbonate is mainly calcite (Supplemental Figure 4; Figure 8C).

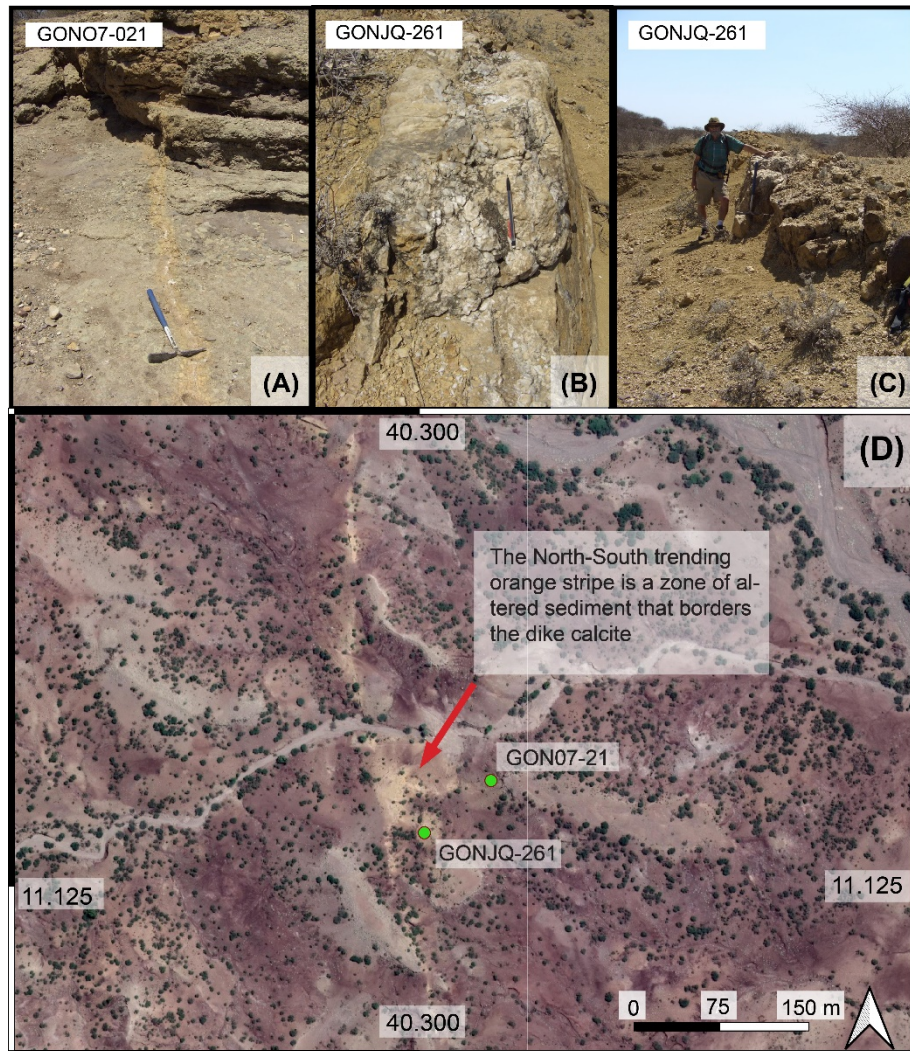### 4.1.3. Hydrothermal Carbonates

Figure 9: Representative field photos of hydrothermal carbonates in the Afar. A) Vein calcite with a 60 cm long pick for scale. B) Dike calcite with pencil for scale. C) Large dike calcite with a person for scale. D) A Google Earth image of the locations of the high-temperature dike calcites. In A, B, and C, note the orange sediment, indicating hydrothermal alteration.

Dike calcites (n=2):

These carbonates are calcite-filled dikes and veins that crosscut the western exposures of the Sagantole Fm, west of the As Duma Fault, where there are distinct zones of altered sediment surrounding the dikes and veins (Figures 1, 9). In one sample (GONJQ-261), cloudy white aggregates of large euhedral and anhedral calcite crystals are 5 – 10 cm across. In the other sample (GON07-21), the small crystals intertwine with small bands of clay to silt-sized grains, with the small crystals of calcite measuring 1 – 3 cm centimeters in width. XRD data indicate both hydrothermal carbonates are calcite supplemental materials.
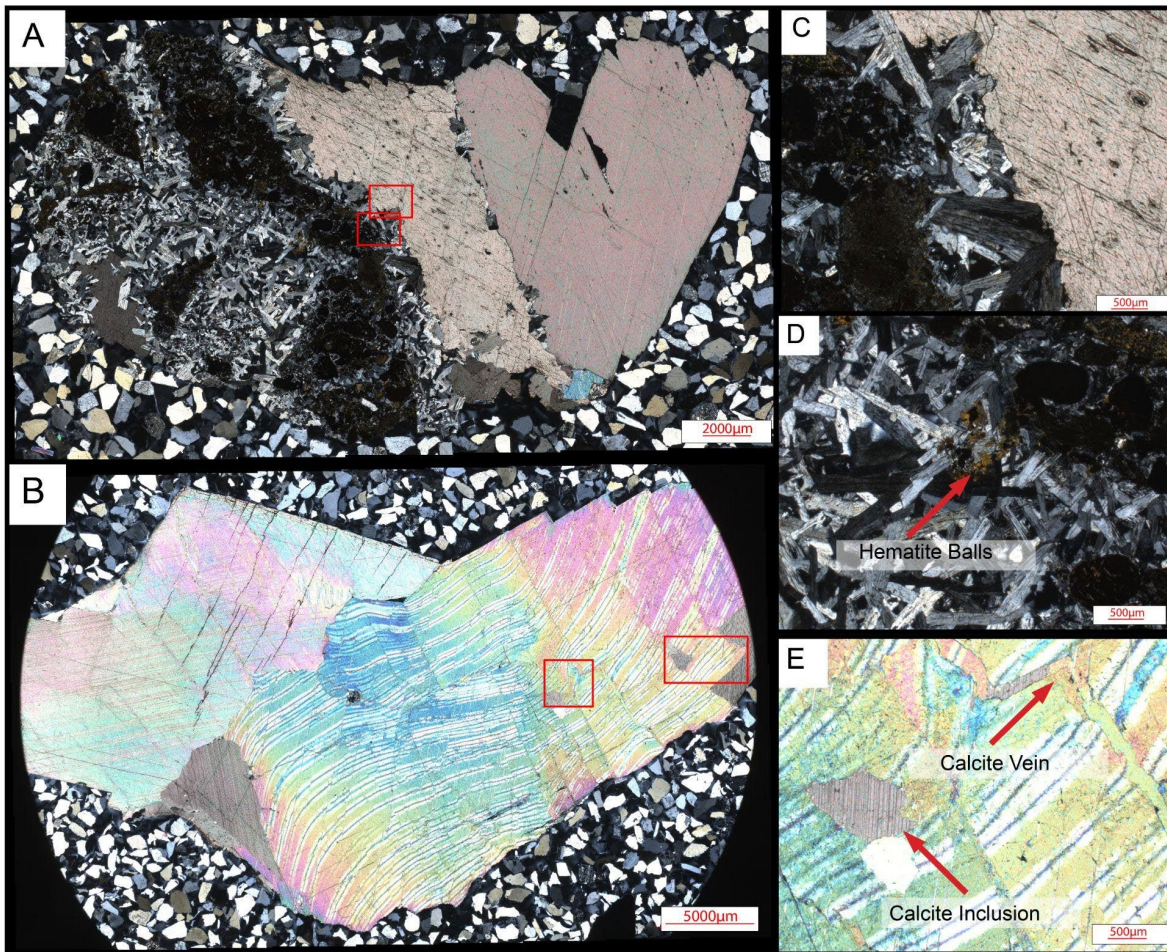

Figure 10: Representative cross-polarized light images of hydrothermal calcites. A) Calcite GON07-021. The red rectangle represents the section where photos C and D are found. B) Mosaic photo of GONJQ-261. Full calcite crystal formed after the slight inclusions of calcite stuck in the crystal. The red rectangle represents the section where photos E and F are found. C) Close-up showing the boundary between the calcite that intruded into the rock and the low birefringence minerals with hematite balls. D) The low birefringence mineral and the surrounding hematite balls. E) Calcite inclusion and a small calcite vein.

4.2. Stable Isotope Geochemistry of Carbonates

The $\delta^{13}C$, $\delta^{18}O_{carbonate}$, and Δ_{47} values for the carbonates in this study are reported in Table 5, along with the corresponding reconstructed Δ_{47}-temperatures and $\delta^{18}O_{pw}$ values. A summary of the $\delta^{18}O_{carbonate}$ and Δ_{47} values, grouped by the three broad carbonate categories introduced in Section 3.1 (Table 4), are in the text below and reported in Table 6. The $\delta^{13}C$ data are not discussed as they are not a focus of this study, but they are available for all samples as they are generated along with the $\delta^{18}O_{carbonate}$ and Δ_{47} data and are

reported in Table 5. The reported error is the standard deviation of the mean isotopic values for each category. Reported $\delta^{18}O_{carbonate}$ values use the VPDB scale, while reported reconstructed $\delta^{18}O_{pw}$ values use the VSMOW scale. All carbonate reported Δ_{47} compositions use the CDES90 scale.

4.2.1. Afar Carbonates $\delta^{18}O_{carbonate}$ and Δ_{47} isotopic compositions

Depositional carbonates (pedogenic nodules, marls, concretions, carbonate ledges) yield $\delta^{18}O_{carbonate}$ values that average -7.0 ± 2.0 ‰ and range from $-13.1 – -3.2$ ‰ (n = 55, Figure 11A). Carbonate Δ_{47} values yield a mean of 0.652 ± 0.04 ‰ and range from $0.507 – 0.698$‰, corresponding to temperatures that range from $20 – 61$ ˚C (Tables 5 – 6). Post-depositional carbonates yield average $\delta^{18}O_{carbonate}$ values of -9.9 ± 3.6 ‰ and range from $-14.8 – -5.6$ ‰ (n = 10). Carbonate Δ_{47} values from these carbonates yield means of 0.543 ± 0.04 ‰, ranging from $0.477 – 0.597$ ‰, corresponding to the largest range of temperatures ($27 – 74$ ˚C) (Figure 11B). Hydrothermal carbonates yield the most depleted $\delta^{18}O_{carbonate}$ values among all the samples in this dataset, ranging from $-23.5 – 20.9$ ‰ (n = 2). These samples also yield the lowest Δ_{47} values, ranging from $0.352 – 0.372$ ‰ and corresponding to the highest temperatures among all carbonates we analyzed ($141 – 160$ ˚C) (Figure 11B).

4.2.2. $\delta^{18}O$ of reconstructed waters

The oxygen isotope values of the parent waters ($\delta^{18}O_{pw}$) for these carbonates are reconstructed using $\delta^{18}O_{carbonate}$ values and Δ_{47} temperatures for each sample, assuming an equilibrium relationship between the isotopic composition of calcite and the water from which it precipitates (see Methods). Depositional carbonates yield the largest range in $\delta^{18}O_{pw}$ values ($-7.7 – -0.5$ ‰) and average -3.1 ± 1.6 ‰. Among the depositional carbonates, the pedogenic carbonates are responsible for the large range of $\delta^{18}O_{pw}$ values; all other types of depositional carbonates (i.e., marls, concretions, carbonate ledges) span a smaller range in $\delta^{18}O_{pw}$ values (Table 6, Figure 11C). Post-depositional carbonates yield mean $\delta^{18}O_{pw}$ values of -3.7 ± 1.3 ‰, ranging from $-5.3 – -1.8$ ‰ (n = 10). The two samples in the hydrothermal carbonate category yield a mean $\delta^{18}O_{pw}$ value of -2.2 ± 0.6 ‰ (Figure 11C).

5. Discussion

When grouped by the three broad carbonate types, there are distinctions in $\delta^{18}O_{carbonate}$ values and Δ_{47}-temperatures. Depositional carbonates yield the highest $\delta^{18}O_{carbonate}$ values and lowest Δ_{47}-temperatures, whereas hydrothermal carbonates yield the lowest $\delta^{18}O_{carbonate}$ values and high Δ_{47}-temperatures, with post-depositional carbonates falling in between (Figure 11B). The apparent covariation between $\delta^{18}O_{carbonate}$ values and Δ_{47} temperatures reflects the strong temperature dependence of oxygen isotope fractionation during equilibrium precipitation of calcite from water (see Eq 4). The elevated heat flow of Afar seems to be a large factor driving the variation of $\delta^{18}O_{carbonate}$; see Section 5.2 for further discussion of variation in observed $\delta^{18}O_{carbonate}$ values. Viewed in very general terms, the distinctions in Δ_{47}-temperatures among these carbonate types are clear; carbonates that form at near-surface conditions during deposition have cooler temperatures than carbonates that form when a rock is buried and influenced by elevated temperatures associated with higher geothermal gradients or hydrothermal activity. However, it is important to consider variation in Δ_{47}-temperatures within these carbonate groupings and to evaluate whether these Δ_{47}-temperatures make sense in terms of the current understanding of temperatures in rift and tectonically active settings.

Table 5: Geochemical data including stable and clumped-isotope compositions. Samples are listed by Locality and Sample ID

Lab	Sample ID	Stratigraphy	Specific Carbonate Type	$\delta^{18}O$ (‰, VPDB) mean	1σ	$\delta^{13}C$ (‰, VPDB) mean	1σ	Δ_{47} (CDES90)[A] mean	1σ	Δ_{47}-temperatures (˚C)[B] mean	1σ	$\delta^{18}O_{pw}$ (‰, SMOW)[C] mean	1σ	Replicates
DEPOSITIONAL														
JHU	WM11-MRV-118	Woranso-Mille	Carbonate Ledge	-4.9	0.04	-6.0	0.00	0.570	0.02	36	7.8	-0.5	1.47	2
JHU	WM11-ARI-134	Woranso-Mille	Carbonate Ledge	-6.8	0.04	-1.9	0.04	0.554	0.01	41	2.8	-1.3	0.48	2
UM	WM18-KSA-275x-1A	Woranso-Mille	Carbonate Ledge	-4.9	0.15	-3.6	0.06	0.589	0.03	29	9.0	-1.7	1.92	4
UM	WM18-KSA-275x-1B	Woranso-Mille	Carbonate Ledge	-9.7	0.04	-6.3	0.03	0.546	0.02	44	7.9	-3.7	1.40	4
UM	WM18-MRD-415A	Woranso-Mille	Marl	-8.7	0.05	-6.3	0.08	0.589	0.01	29	2.8	-5.6	0.54	4
UM	WM18-MRD-217A	Woranso-Mille	Marl	-8.4	0.56	-7.0	0.02	0.542	0.02	46	6.5	-2.2	1.65	4
UM	WM18-MRD-215A	Woranso-Mille	Marl	-6.6	0.49	-7.2	0.15	0.544	0.03	46	13.6	-0.4	2.87	4
UM	WM18-MRD-213A	Woranso-Mille	Marl	-6.7	0.63	-7.1	0.06	0.557	0.02	40	7.6	-1.4	1.93	4
UM	WM18-MRD-224A	Woranso-Mille	Marl	-8.1	0.10	-7.0	0.05	0.546	0.02	44	8.1	-2.1	1.55	4
UM	WM18-LHG-253A	Woranso-Mille	Marl	-7.8	0.02	-6.7	0.02	0.546	0.01	44	3.9	-1.9	0.69	4
UM	WM18-LHG-252A	Woranso-Mille	Marl	-8.0	0.02	-6.7	0.04	0.551	0.01	42	5.3	-2.4	0.92	4
UM	WM18-LHG-251A	Woranso-Mille	Marl	-8.7	0.05	-7.0	0.03	0.593	0.02	28	6.5	-5.8	1.39	4
UM	WM18-MRD-232A	Woranso-Mille	Marl	-9.2	0.03	-7.8	0.04	0.554	0.01	41	2.8	-3.7	0.59	4
UM	WM18-MRD-231A	Woranso-Mille	Marl	-7.6	0.63	-7.5	0.05	0.563	0.01	38	4.5	-2.8	1.42	4
JHU	DANL-106a	Busidima	Pedogenic Carbonate	-7.4	0.15	-5.1	0.01	0.574	0.00	34	0.0	-3.3	0.08	2
JHU	DANL-108a	Busidima	Pedogenic Carbonate	-7.3	0.00	-5.5	0.00	0.574	0.00	34	0.0	-3.2	0.00	2
JHU	DANL-111a	Busidima	Pedogenic Carbonate	-8.7	0.08	-3.1	0.01	0.570	0.00	35	1.4	-4.4	0.35	2
JHU	DANL-115a	Busidima	Pedogenic Carbonate	-10.1	0.21	-2.1	0.08	0.601	0.01	25	2.8	-7.7	0.39	2
JHU	DANL-129	Busidima	Pedogenic Carbonate	-6.9	0.33	-2.6	0.53	0.611	0.01	22	4.2	-5.2	1.20	2
JHU	DANL-3	Busidima	Pedogenic Carbonate	-5.8	0.15	-6.9	0.01	0.577	0.00	33	0.0	-1.9	0.27	2
JHU	DANL-37	Busidima	Pedogenic Carbonate	-6.7	0.13	-6.3	0.03	0.593	0.01	28	2.1	-3.8	0.20	2
JHU	DANL-4	Busidima	Pedogenic Carbonate	-5.4	0.16	-6.4	0.86	0.593	0.03	28	8.5	-2.4	1.80	2
JHU	DANL-40	Busidima	Pedogenic Carbonate	-8.0	0.09	-3.2	0.02	0.607	0.00	24	0.7	-6.0	0.25	2
JHU	DANL-80	Busidima	Pedogenic Carbonate	-6.2	0.21	-6.1	0.03	0.583	0.02	31	7.1	-2.6	1.05	2
JHU	DANL-96	Busidima	Pedogenic Carbonate	-5.4	0.16	-5.1	0.02	0.576	0.02	34	7.8	-1.4	1.23	2
JHU	GONJQ-136	Busidima	Pedogenic Carbonate	-3.2	0.16	-5.3	0.03	0.618	0.01	20	2.8	-1.9	0.65	2
JHU	GONJQ-137	Busidima	Pedogenic Carbonate	-5.0	0.12	-5.7	0.02	0.605	0.01	24	1.4	-2.9	0.44	2
JHU	GONJQ-18	Hadar	Pedogenic Carbonate	-8.3	0.06	-6.6	0.02	0.583	0.01	31	2.1	-4.8	0.52	2
JHU	GONJQ-20	Hadar	Pedogenic Carbonate	-7.2	0.06	-7.0	0.02	0.567	0.00	36	0.0	-2.6	0.04	2
JHU	GONJQ-202	Busidima	Pedogenic Carbonate	-5.4	0.19	-5.7	0.06	0.593	0.00	28	0.7	-2.5	0.30	2
JHU	GONJQ-204	Busidima	Pedogenic Carbonate	-6.1	0.17	-0.9	0.06	0.592	0.00	28	1.4	-3.1	0.40	2
JHU	GONJQ-230	Busidima	Pedogenic Carbonate	-5.9	0.16	-5.6	0.01	0.591	0.00	28	0.0	-2.9	0.17	2
JHU	GONJQ-242	Sagantole	Pedogenic Carbonate	-11.9	0.23	-10.0	0.03	0.535	0.01	48	4.2	-5.2	1.01	2
JHU	GONJQ-266	Busidima	Pedogenic Carbonate	-4.8	0.14	-2.9	0.06	0.604	0.01	24	4.2	-2.7	1.04	2
JHU	GONJQ-268	Busidima	Pedogenic Carbonate	-3.8	0.10	-4.7	0.05	0.598	0.01	26	2.8	-1.2	0.49	2
JHU	GONJQ-284	Busidima	Pedogenic Carbonate	-4.1	0.01	-5.4	0.04	0.613	0.02	22	5.0	-2.4	1.00	2
JHU	GONJQ-31	Hadar	Pedogenic Carbonate	-9.9	0.01	-4.6	0.08	0.577	0.00	33	1.4	-6.0	0.28	2
JHU	GONJQ-316	Hadar	Pedogenic Carbonate	-7.5	0.17	-10.1	0.16	0.595	0.02	27	5.7	-4.7	1.34	2
JHU	GONJQ-36a	Hadar	Pedogenic Carbonate	-5.4	0.16	-4.6	0.01	0.610	0.00	23	0.7	-3.5	0.29	2
JHU	GONJQ-37	Hadar	Pedogenic Carbonate	-4.6	0.04	-6.3	0.07	0.574	0.01	34	4.2	-0.5	0.76	2
JHU	GONJQ-57	Busidima	Pedogenic Carbonate	-6.7	0.13	-6.0	0.03	0.567	0.02	37	7.8	-2.1	1.50	2
JHU	GONJQ-64	Busidima	Pedogenic Carbonate	-6.4	0.12	-4.3	0.04	0.576	0.00	33	1.4	-2.5	0.40	2
JHU	GONJQ-78	Busidima	Pedogenic Carbonate	-7.5	0.11	-0.6	0.05	0.591	0.01	28	2.8	-4.5	0.60	2
JHU	GONJQ-7a	Busidima	Pedogenic Carbonate	-6.4	0.08	-5.6	0.02	0.579	0.01	33	2.1	-2.6	0.47	2

Lab	Sample ID	Stratigraphy	Specific Carbonate Type	δ¹⁸O (‰, VPDB) mean	1σ	δ¹³C (‰, VPDB) mean	1σ	Δ₄₇ (CDES90)[A] mean	1σ	Δ₄₇- temperatures (˚C)[B] mean	1σ	δ¹⁸O_pw (‰, SMOW)[C] mean	1σ	Replicates
JHU	GONJQ-83	Busidima	Pedogenic Carbonate	-5.3	0.13	-3.3	0.04	0.578	0.01	33	3.5	-1.4	0.77	2
JHU	GONJQ-84	Busidima	Pedogenic Carbonate	-4.7	0.15	-5.0	0.04	0.596	0.03	27	8.5	-2.0	1.84	2
JHU	GONJQ-99a	Busidima	Pedogenic Carbonate	-6.2	0.19	-5.2	0.04	0.580	0.01	32	4.2	-2.5	1.04	2
JHU	GONNL-38	Hadar	Pedogenic Carbonate	-6.7	0.03	-6.4	0.02	0.560	0.00	39	0.0	-1.6	0.01	2
JHU	GONNL-40	Hadar	Pedogenic Carbonate	-3.8	0.01	-5.0	0.01	0.586	0.00	30	1.4	-0.5	0.26	2
JHU	WM11-ARI-125	Woranso-Mille	Pedogenic Carbonate	-8.4	0.08	-5.4	0.00	0.550	0.01	43	3.5	-2.7	0.49	2
JHU	WM11-ARI-129	Woranso-Mille	Pedogenic Carbonate	-7.0	0.00	-6.5	0.02	0.573	0.03	35	10.6	-2.8	2.09	2
JHU	GONJQ-10	Busidima	Pedogenic Carbonate	-6.8	0.16	-4.2	0.03	0.584	0.02	31	5.7	-3.3	1.25	2
UM	GONJQ-294-3A	Sagantole	Radial Concretion	-13.1	0.04	-7.3	0.03	0.507	0.04	61	19.3	-4.5	3.10	4
JHU	WM11-KSA-162	Woranso-Mille	Radial Concretion	-8.4	0.01	-5.0	0.01	0.566	0.02	37	6.4	-3.8	1.22	2
UM	WM11-LDD-142-2A	Woranso-Mille	Radial Concretion	-8.7	0.10	-7.0	0.03	0.524	0.03	53	10.2	-1.2	1.69	4
HYDROTHERMAL														
JHU	GON07-21	Sagantole	Dike Calcite	-20.9	0.11	-7.2	0.01	0.372	0.01	141	7.1	-1.8	0.81	2
UM	GONJQ-261-4A	Sagantole	Dike Calcite	-23.5	0.12	-7.4	0.03	0.352	0.01	160	9.0	-2.6	0.90	4
POST-DEPOSITIONAL														
JHU	WM11-ARI-135	Woranso-Mille	Basalt Calcite	-8.3	0.12	-4.5	0.01	0.547	0.02	44	7.8	-2.3	1.28	2
UM	GONJQ-076-5A	Sagantole	Euhedral Calcite-Bone	-6.1	0.01	-2.3	0.01	0.597	0.00	27	0.7	-3.5	0.23	4
UM	GONJQ-250-6A	Sagantole	Euhedral Calcite-Bone	-14.8	0.10	-6.8	0.06	0.488	0.01	69	6.4	-4.8	0.82	4
UM	GONJQ-258-8A	Sagantole	Euhedral Calcite-Bone	-13.7	0.07	-5.6	0.02	0.477	0.02	74	10.4	-2.8	1.43	4
UM	GONJQ-260-7A	Sagantole	Euhedral Calcite-Bone	-12.5	0.07	-5.7	0.05	0.527	0.02	52	9.0	-5.3	1.59	4
JHU	WM11-MSD-102	Woranso-Mille	Fault Calcite	-7.5	0.28	-4.6	0.03	0.568	0.01	36	2.8	-3.0	0.78	2
JHU	GONJQ-103	Busidima	Gravel Cement	-5.5	0.16	-4.2	0.04	0.580	0.01	32	2.1	-1.8	0.56	2
UM	GONJQ-139-9A	Busidima	Spar Infill	-6.7	0.18	-6.8	0.02	0.581	0.04	32	14.7	-3.0	2.87	4
JHU	GON07-48	Sagantole	Spar Infill	-14.3	0.01	-7.9	0.01	0.502	0.00	62	1.4	-5.3	0.16	2
JHU	GONNL-35	Sagantole	Spar Infill	-10.1	0.01	-6.8	0.00	0.560	0.00	39	0.0	-5.0	0.01	2

[A]Samples were analyzed using the Carbon Dioxide Equilibrium Scale (CDES) at 90˚C.

[B]The Δ₄₇ isotopic values at 90˚C were converted into temperature values using the calibration equation for carbonates from Bonifacie et al. (2017).

[C]Reconstructed δ¹⁸O_pw values were calculated from δ¹⁸O_carbonate values and Δ₄₇ derived temperatures, assuming equilibrium fractionation during the formation of calcite from water, following the equation for equilibrium fractionation from Kim and O'Neil (1997), where T is the temperature in Kelvin: Eq (4):$1000\ln\alpha_{calcite-H2O} = (18.03 \times 10^{3}/T) - 32.42$

and $\alpha_{calciteH2O}$ is the fractionation factor for calcite formed in equilibrium with water which can reconstruct the δ¹⁸O of the parent water.

Eq (5):$\alpha_{calcite-H2O} = (1000 + \delta^{18}O_{calcite})/(1000 + \delta^{18}O_{water})$

Table 6. Summary of isotopic data by carbonate type

Carbonate Category	count	δ¹⁸O$_{carbonate}$ (‰, VPDB)				Δ$_{47}$ (CDES90) (‰)[A]				Δ$_{47}$ Temperature (˚C)[B]				δ¹⁸O$_{pw}$ (‰, SMOW)[C]			
		mean	1σ	min	max	mean	1σ	min	max	mean	1σ	min	max	mean	1σ	min	max
Depositional Carbonates	55	-7.0	1.96	-13.1	-3.2	0.5759	0.02	0.507	0.618	34	8.30	20	61	-2.9	1.58	-7.7	-0.4
Pedogenic Nodules	38	-6.5	1.80	-11.9	-3.2	0.585	0.02	0.535	0.618	31	5.90	20	48	-3.1	1.60	-7.7	-0.5
Marls	10	-8.0	0.84	-9.2	-6.6	0.5585	0.02	0.542	0.593	40	6.48	28	46	-2.8	1.73	-5.8	-0.4
Radial Concretions	3	-10.1	2.70	-13.1	-8.4	0.532	0.03	0.507	0.566	50	12.20	37	61	-3.2	1.70	-4.5	-1.2
Carbonate Ledge	4	-6.6	2.30	-9.7	-4.9	0.565	0.02	0.546	0.589	38	6.60	29	44	-1.8	1.40	-3.7	-0.5
Post-Depositional Carbonates	10	-10.0	3.60	-14.8	-5.5	0.543	0.04	0.477	0.597	47	16.70	27	74	-3.7	1.30	-5.3	-1.8
Basalt Calcite	1	-8.3	0.10	N/A	N/A	0.547	0.02	N/A	N/A	44	7.80	N/A	N/A	-2.3	1.30	N/A	N/A
Gravel Cement	1	-5.5	0.20	N/A	N/A	0.58	0.01	N/A	N/A	32	2.10	N/A	N/A	-1.8	0.60	N/A	N/A
Bone Infill	4	-11.8	3.90	-14.8	-6.1	0.522	0.05	0.477	0.597	56	21.20	27	74	-4.1	1.10	-5.3	-2.8
Spar Infill	3	-10.4	3.80	-14.3	-6.7	0.548	0.04	0.502	0.581	44	15.70	32	62	-3.9	2.20	-5.3	-1.3
Fault Carbonate	1	-7.5	0.30	N/A	N/A	0.568	0.01	N/A	N/A	36	2.80	N/A	N/A	-4.4	1.30	-5.3	-3
Hydrothermal Carbonates	2	-22.2	1.80	-23.5	-20.9	0.362	0.01	0.352	0.372	151	13.40	141	160	-2.2	0.60	-2.6	-1.8

[A]Samples were analyzed using the Carbon Dioxide Equilibrium Scale (CDES) at 90˚C.

[B]The Δ$_{47}$ isotopic values at 90˚C were converted into temperature values using the calibration equation for carbonates from Bonifacie et al. (2017).

[C]Reconstructed δ¹⁸O$_{pw}$ values were calculated from δ¹⁸O$_{carbonate}$ values and Δ$_{47}$ derived temperatures, assuming equilibrium fractionation during the formation of calcite from water, following the equation for equilibrium fractionation from Kim and O'Neil (1997), where T is the temperature in Kelvin: Eq (4):$1000\ln\alpha_{calcite-H2O} = (18.03 \times 10^3/T) - 32.42$

and $\alpha_{calciteH2O}$ is the fractionation factor for calcite formed in equilibrium with water which can reconstruct the δ¹⁸O of the parent water.

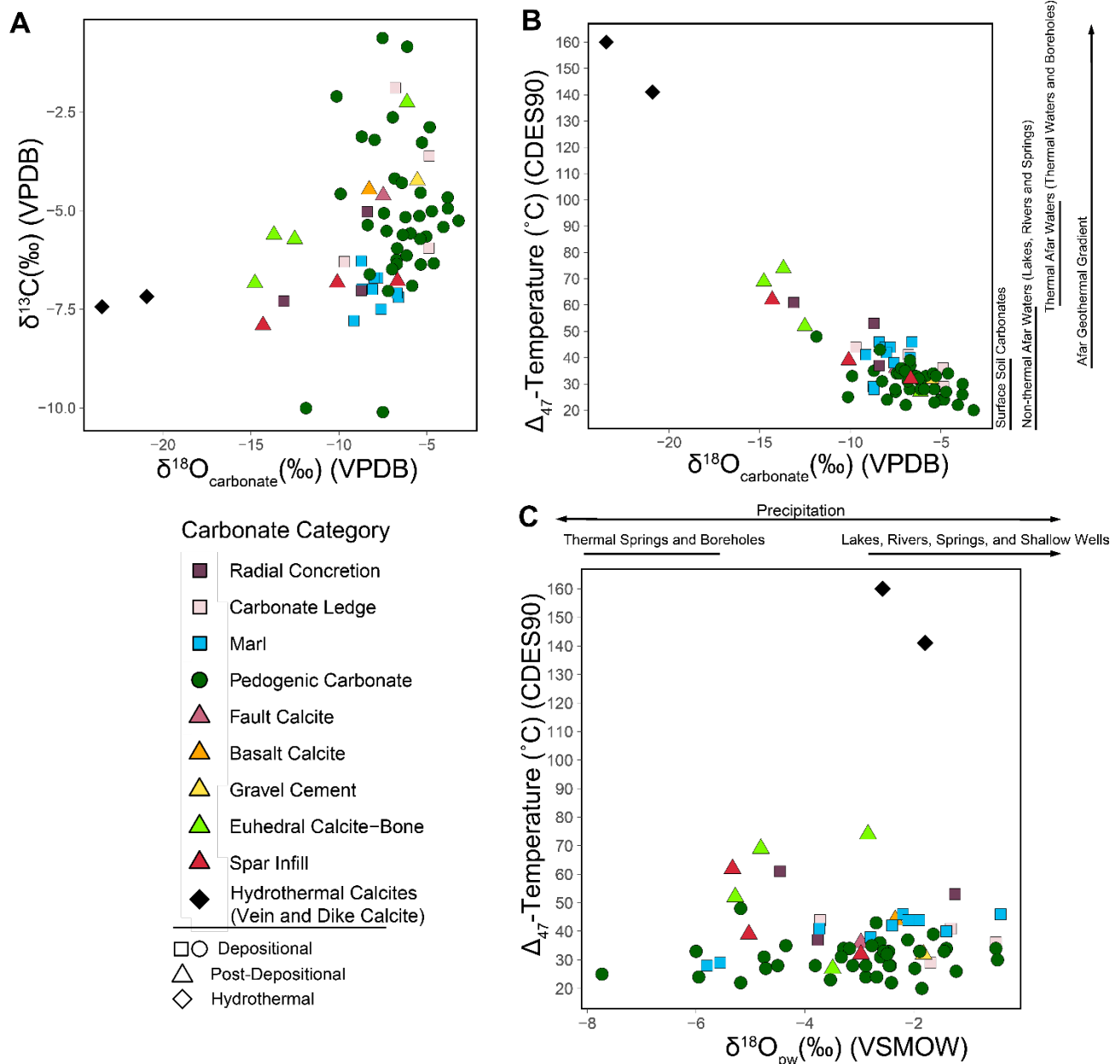Eq (5):$\alpha_{calcite-H2O} = (1000 + \delta^{18}O_{calcite})/(1000 + \delta^{18}O_{water})$

Figure 11: Stable isotopic values by carbonate category. The values reported for each sample are an average of replicate analyses. A) A cross plot of $\delta^{13}C$ and $\delta^{18}O_{carbonate}$ values. B) Δ_{47} temperatures and $\delta^{18}O_{carbonate}$ values with black scale bars on the right marking the temperature ranges observed in comparative settings. Data that inform these bars come from the following sources: soil and Δ_{47}-temperatures from modern pedogenic carbonates in eastern Africa (Passey et al., 2010; Beverly et al., 2021), surface water temperatures for thermal and non-thermal waters from the Afar (see Table 2 for citations), and the range of geothermal gradient temperatures in the Afar for the first kilometer (see Table 3 for citations). C) Carbonate Δ_{47}-temperatures and $\delta^{18}O_{pw}$ values with black horizontal lines at the top of the plot indicate published ranges of $\delta^{18}O$ of waters in the Afar (Levin et al., 2009; Alemayehu et al., 2017; Bedaso et al., 2020; Kebede et al., 2021). The full range of observed precipitation $\delta^{18}O$ values exceeds the limits of this plot, spanning -12.6 ‰ to +10.3 ‰ (Bedaso et al., 2020). Arrows indicate when the ranges extend past the axes of the plots in B and C; $\delta^{18}O$ values of precipitation, meteoric waters, and surface waters extend to +10.3 ‰, while the Afar gradient temperatures extend to 190 °C/km.

5.1. Summary of temperature distributions considering carbonate forms and geologic context

Depositional Carbonates

For depositional carbonates, we expect them to form at temperatures that are typical of near-surface conditions. In the Afar, soil temperatures can reach up to 40 ˚C (Passey et al. 2010), and the temperatures of surface waters and near surface groundwater (not influenced by hydrothermal waters) can range from 20 – 60 ˚C. Among the depositional carbonates, pedogenic carbonates (30.6 ± 5.9 ˚C, n = 38) and marls (40 ± 6.5 ˚C, n = 10) yield the lowest temperatures (Figure 11B). All except for two pedogenic nodules yield Δ_{47}-temperatures < 40 ˚C, which is consistent with their formation during deposition and how they track near-surface conditions. As discussed more thoroughly in the background (Section 2.4), this rough threshold of 40 ˚C for pedogenic carbonates is consistent with Δ_{47}-temperatures from other Pliocene and Pleistocene pedogenic carbonates sampled in eastern Africa (Passey et al., 2010; Ludecke et al. 2018). The pedogenic nodules that yield Δ_{47}-temperatures near or above 40 ˚C are discussed later in this paper. Carbonate ledges yield Δ_{47}-temperatures that range from 29 to 44 ˚C. Within the single sample WM18-KSA-275X, the fibrous calcite yields a higher temperature (44 ± 8 ˚C) than the micrite portion (29 ± 9 ˚C) (see Figures 3D and 7 for the distinctions within this sample), which suggests increases in temperature after initial deposition. The concretions yield the highest temperatures among the depositional carbonates (37.5 ± 6.6 ˚C, ranging from 37 – 61 ˚C, n = 3); those with elevated temperatures (> 40 ˚C) likely represent the influence of post-depositional processes on carbonate formation. This observation indicates some of these carbonates may not be depositional and need reclassification.

Post-Depositional Carbonates

The post-depositional carbonates yield a wide range of temperatures from 27 – 74 ˚C (46.7 ± 16.7 ˚C, n = 10), where the samples with Δ_{47}-temperatures < 40 ˚C are consistent with formation in surface environments. Samples with higher temperatures may reflect the influence of hydrothermal waters or increased temperatures from burial. Surface waters (lakes, rivers, springs) in the Afar with clear hydrothermal influence can be up to 60 ˚C, with thermal springs reaching temperatures of 100 ˚C, and boreholes in the Afar show that temperatures at >2 km can reach 200 ˚C (Zan et al., 1990; Gizaw., 1996; Houssein et al., 2013; Minissale et al., 2017; Chandrasekharam et al., 2019; Bekele et al., 2021, Table 2).

Hydrothermal Carbonates

Calcite samples from veins and dikes associated with zones of hydrothermal alteration in the Sagantole Fm at Gona (Figure 9) yield the highest Δ_{47}-temperatures from this study. These calcites yield temperatures of 141 ± 7 ˚C and 160 ± 9 ˚C. These temperatures exceed those observed in hydrothermal springs in the Afar (Table 2); however, they are within the range of temperatures observed for the Afar, where the geothermal gradient can increase to 190 °C/km and temperatures exceed 350 ˚C at 2 km depth (Zan et al., 1990; Gizaw., 1996; Houssein et al., 2013; Minissale et al., 2017; Chandrasekharam et al., 2019; Bekele et al., 2021, Table 1). Sediments surrounding the dike calcite have orange staining indicative of hydrothermal alteration (Figure 9) consistent with these high temperatures. These high temperatures likely indicate that these dikes and veins formed > 1 to 2 km depth and have been uplifted. More work needs to be done to understand the exact formation for these samples, but this general interpretation is consistent with the geologic setting for these samples; they are from veins and dikes that cut through the Sagantole Fm (>4.6–3.9 Ma), which is heavily faulted, bounded by basalts and contains extensive indications of hydrothermal activity (Figures 1B, 2, 9). Petrographic images indicate the dike carbonates are predominantly calcite with smaller calcite inclusions showing re-precipitation events (Figures 10B, 10E, 10F).

Geological Context

Based on the geological context and isotopic composition of the depositional carbonates, most carbonates from the Hadar Fm, the Busidima Fm, and Woranso-Mille formed at surface conditions with little

indication of alteration. Pedogenic carbonates that yield temperatures greater than 40 ˚C (up to 48 ˚C) are all associated with the Sagantole Fm or the ARI area of Woranso-Mille where there is fault activity or possible burial (sample is approximate ~3.59 Ma). The post-depositional carbonates (i.e., fault calcite, gravel cement, bone calcites, and spar infill) exhibit the largest temperature variation (27 – 74 ˚C) of the three carbonate groupings. The void-filling carbonates from the Hadar and Busidima Fms at Gona and those from Woranso-Mille yield Δ_{47}-temperatures that range from 27 – 44 °C. In contrast, void-filling carbonates that yield higher temperatures (52 – 74 ˚C) are all from the Sagantole Fm (Figures 11B, 12), where there is clear evidence for hydrothermal alteration of the sediments and extensive faulting. Examining carbonates based on their geological context, we see clear indications that the Sagantole Fm carbonates are much higher in Δ_{47}-temperatures (48 – 160 °C) compared to those from Gona that are east of the As Duma Fault (Hadar and Busidima Fms) and to Woranso-Mille carbonates (Figure 12). From these initial observations, the influence of high-temperature processes (where carbonate formation temperatures > 50˚C) is restricted to areas where there are clear indications of hydrothermal activity and extensive faulting (Figure 12).
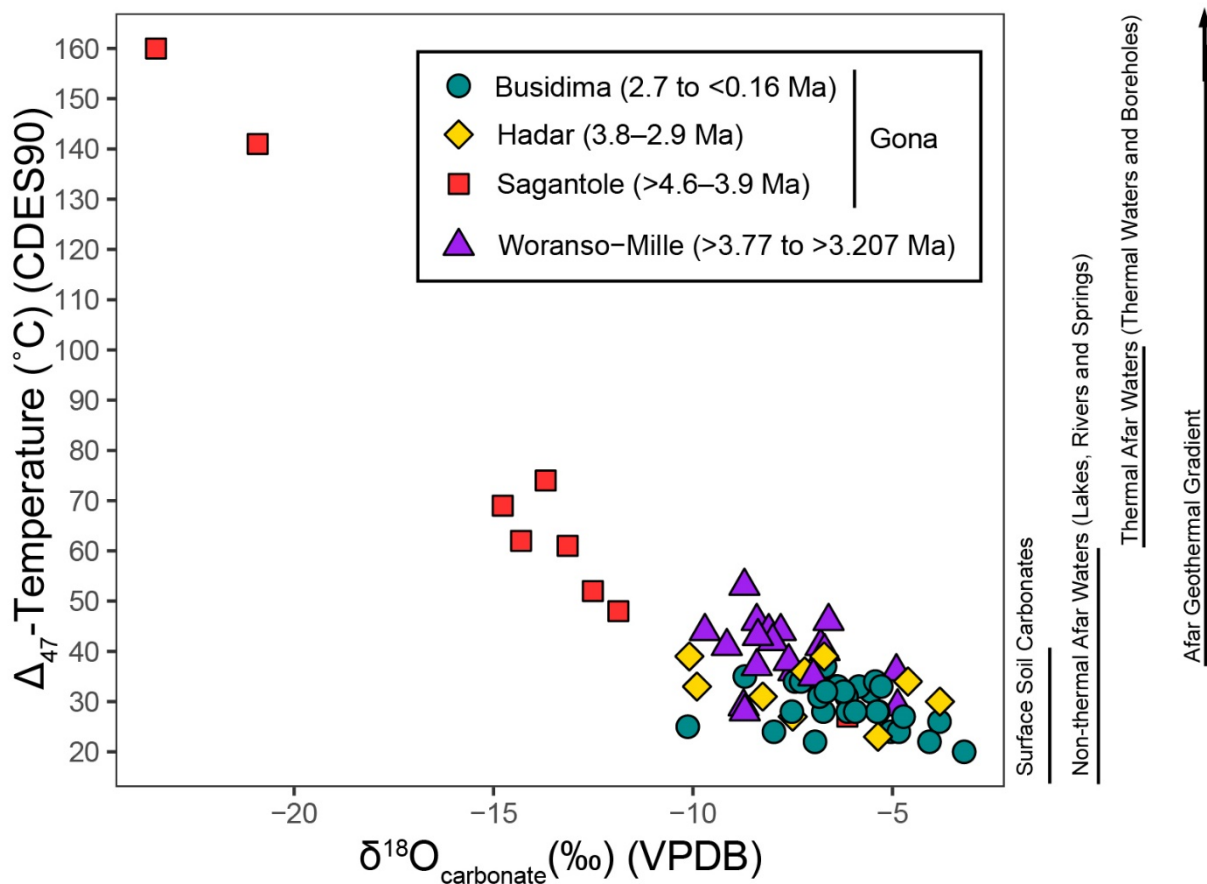
Figure 12: Carbonate $\delta^{18}O$ and Δ_{47} temperatures as plotted in Figure 11A but with data points grouped by general geologic context instead of carbonate category. See the caption for Figure 11A for references for temperature ranges listed to the right of the plot. Unlike Gona, the Woranso-Mille samples are not differentiated into separate units.

5.1.1. Afar carbonate Δ_{47} temperatures compared to other Δ_{47} studies

Carbonate Δ_{47}-temperatures and $\delta^{18}O_{carbonate}$ values found in Pliocene and Pleistocene strata record high heat and indicate the influence of hydrothermal sources, volcanism, and fault activity. However, the

influence of high heat is localized in certain areas rather than throughout Woranso-Mille and Gona. Most carbonate temperatures match surface soil carbonate and thermal and non-thermal water temperatures; however, the hydrothermal carbonates may represent formation at depths below the surface, or the high geothermal gradients in some areas of the Afar, creating Δ_{47} carbonate temperatures $\geq 140°C$.

The majority of Δ_{47}-temperatures from the Afar carbonates overlap with results from carbonate Δ_{47}-temperatures data reported from other rift settings (Table 3). These other studies, with carbonate Δ_{47}-temperature data from vein calcites and diagenetic carbonates, are from older rift settings (Permian to Miocene; Swanson et al., 2012; Bergman et al., 2013; Hudson et al., 2016; Luetkemeyer et al., 2016; Brigaud et al., 2020; Hoareau et al., 2021). Most rift settings have Δ_{47}-temperatures from $7 – 134°C$, which overlaps with all depositional and void fill carbonates from the Afar (Table 3; Fig 11B). However, the hydrothermal carbonates in this study exceed this range; this is likely because 1) most carbonates studied in other rift systems were vein calcites associated with faults rather than hydrothermal activity, or 2) the thermal gradient is higher in the Afar than in these other rift systems.

5.2. Paleo-fluid reconstructions ($\delta^{18}O_{pw}$)

While Δ_{47} temperatures provide important constraints on conditions of carbonate formation and subsequent alteration, these temperatures also provide additional insights when used with $\delta^{18}O_{carbonate}$ values to reconstruct the oxygen isotopic composition of the parent water ($\delta^{18}O_{pw}$). The large 20 ‰ range in $\delta^{18}O_{carbonate}$ values from the Afar carbonates in this sample set translates to a much smaller range (~7 ‰) in $\delta^{18}O_{pw}$ values. This demonstrates the strong control of temperature on the $\delta^{18}O_{carbonate}$ values of these samples (Figures 11–12). This section reviews reconstructed $\delta^{18}O_{pw}$ values and how these values can help understand carbonate paragenesis in the Afar.

Depositional carbonates are responsible for the full range of $\delta^{18}O_{pw}$ values, with the pedogenic carbonates spanning the full range of $\delta^{18}O_{pw}$ values among all carbonate types (-7.7 – -0.5 ‰; Figure 11C). The $\delta^{18}O_{pw}$ values of the other types of depositional carbonates (e.g., marls, concretions, carbonate ledges) are also variable; there is not a clear distinction between these groups. The $\delta^{18}O_{pw}$ values from all depositional carbonates overlap with $\delta^{18}O$ values of meteoric waters today, showing an extensive range from -12 – +10.3 ‰ (see Section 2.4; Figure 11C). While several studies have examined variation in $\delta^{18}O_{pw}$ values of the depositional carbonates (e.g., Levin et al. 2004; Aronson et al. 2008), these studies do not typically focus on $\delta^{18}O_{pw}$ values from post-depositional and hydrothermal carbonates in the Afar. The $\delta^{18}O_{pw}$ data from the non-depositional carbonates fall within the range of $\delta^{18}O_{pw}$ values of the depositional carbonates. This indicates that non-depositional carbonates form from waters with an isotopic composition similar to $\delta^{18}O$ values of meteoric water from which near-surface carbonates form; there is no indication that the non-depositional carbonates form from non-meteoric fluids. Among modern waters sampled today, thermal waters yield $\delta^{18}O$ values lower than $\delta^{18}O$ values of most meteoric waters (Kebede et al., 2021). Given this, if there were any distinctions in $\delta^{18}O$ values of waters that formed post-depositional carbonates and hydrothermal carbonates, then they would yield values $\delta^{18}O_{pw}$ values that were lower than $\delta^{18}O$ values of meteoric waters. Instead, the $\delta^{18}O_{pw}$ values of post-depositional carbonates and hydrothermal carbonates are fully in the range of $\delta^{18}O_{pw}$ values from depositional carbonates. While it is noteworthy that the $\delta^{18}O_{pw}$ values from hydrothermal carbonates are at the higher end of the range for all reconstructed $\delta^{18}O_{pw}$ values in this dataset (Figure 11C), only two samples have been analyzed, so it is difficult to compare this distribution to that of the large sample size for pedogenic carbonates (n = 38). Our results show no relationship between $\delta^{18}O_{pw}$ and Δ_{47}-temperatures (Figure 11C). In sum, the most prominent trends that come from the $\delta^{18}O_{pw}$ values show the greatest variation in $\delta^{18}O_{pw}$ values among the depositional carbonates and that both the post-depositional carbonates and hydrothermal carbonates fall within the range of $\delta^{18}O$ values from meteoric water, indicating that hydrothermal or fault fluids are likely recycled meteoric waters. This conclusion is consistent with observations of reconstructed $\delta^{18}O_{pw}$ values

from other rift basin carbonates (Bergman et al., 2013; Dale et al., 2014; Hodson et al., 2016; Luetkemeyer et al., 2016; Swanson et al., 2012).

So, what is driving such large variation in the reconstructed carbonate $\delta^{18}O_{pw}$ values? There may be multiple explanations. The pedogenic nodules and marls have a wide range of reconstructed carbonate $\delta^{18}O_{pw}$ values. This is likely due to evaporative influences on parent waters, causing some carbonates to have higher $\delta^{18}O_{pw}$ values. One avenue to constrain or examine carbonate evaporation with $\Delta^{17}O$, which has been proven to help constrain evaporation on carbonates and reconstruct precipitation $\delta^{18}O$ that created the $\delta^{18}O_{pw}$ of the carbonate (Passey and Levin, 2021; Passey and Ji, 2019). Another possibility is that there is variation in $\delta^{18}O$ values of meteoric through time due to climate and hydrological change; we cannot assume that modern waters represent the isotopic composition of water in the Pliocene and Pleistocene. Future work, examining the isotopic data of these carbonates with closer attention to their temporal distribution and geologic context could investigate what drives variation in $\delta^{18}O_{pw}$ values within each carbonate category. For example, the void fill carbonates and the pedogenic carbonates span a considerable time (between 4.5 – 0.8 Ma); sampling carbonates formed during different climate states could explain the large variation in reconstructed carbonate $\delta^{18}O_{pw}$ values.

5.3. What is the influence of hydrothermal activity on the preservation of isotope-based paleoclimate records in the Afar?

While a majority of depositional carbonates yield Δ_{47}-temperatures that fall within the surface temperatures in the Afar (<40 °C) as expected, some carbonates yield higher temperatures (43 – 61 °C). Hydrothermal and post-depositional carbonates associated with the Sagantole Fm strata record elevated temperatures compared to similar carbonates associated with Hadar and Busidima Fms and the majority of samples from Woranso-Mille. To further explore the effect of temperature on controlling the composition of these carbonates, this study examined the petrography of a subset of depositional carbonates. Four pedogenic nodules were selected: one from the Hadar Fm (GONJQ-036a), two from the Sagantole Fm (GONNL-038, GONJQ-242), and one from Woranso-Mille (WM11-ARI-125) (Figure 6). GONJQ-036A, which has Δ_{47}-temperatures of 23 ± 1 °C, had no spar inclusions and was primarily micrite with small hematite inclusions. GONNL-038 and GONJQ-242 yielded Δ_{47}-temperatures of 48 ± 4 °C and 39 ± 0 °C, respectively. GONNL-038 has spar inclusions throughout the brown micrite carbonate, while GONJQ-242 is completely recrystallized with no brown micrite remaining. GONNL-038 and GONJQ-242 are from the Sagantole Fm at Gona, which has altered sediments in association with the As Duma fault, hydrothermal activity, and volcanic activity (Quade et al., 2008) (Figure 1). WM11-ARI-125 had Δ_{47}-temperatures of 43 ± 4 °C, and the pedogenic nodule had spar surrounding the original micrite material under the petrographic microscope. One possible reason for the elevated temperatures is that WM11-ARI-125 is nearby (>1 km) a fault in line with clear carbonate formation infilling it (represented by sample WM11-MSD-102), which may have introduced fluids into the area at the time of its movement. Based on the context of these carbonates, it is clear that hydrothermal activity (associated with volcanism and faults) may have influenced the $\delta^{18}O_{calcite}$ values and Δ_{47}-temperatures of some of these carbonates. Most of the depositional carbonates seem to form at temperatures <40 °C, but there is potential for high-temperature fluids to alter the carbonates, as clear from both the Δ_{47} temperatures and the petrographic investigation showing spar and recrystallization of some of the pedogenic carbonates from the Sagantole Fm. However, elevated Δ_{47}-temperatures of the depositional carbonates seem localized to places with other indications of high heat (e.g., field indications of hydrothermal activity, petrographic indications of spar and replacement calcite, void calcite with high Δ_{47}-temperatures). This suggests that with a thorough examination of geologic context, petrography, and clumped isotope thermometry of different carbonate forms, it is possible to assess the effect of elevated temperatures on the isotopic composition of depositional carbonates and evaluate their fidelity as archives of paleoenvironmental change.

Conclusion

Combining clumped isotope thermometry, petrographic analysis, and XRD data, this study has investigated 1) whether the carbonate sedimentary strata in the Afar Rift contain a record of high temperatures of the Afar triple junction and 2) the influence of these temperatures on the carbonate stable isotope records usually used for paleoenvironmental reconstruction. The Δ_{47}-temperatures and $\delta^{18}O_{carbonate}$ samples studied for this thesis record the elevated temperatures in carbonates that are associated with local hydrothermal activity near areas of volcanic activity and faulting. Carbonates that are directly associated with field evidence for hydrothermal activity (i.e., calcite-filled dikes and veins that cut through zones of hydrothermally altered sediment) yield temperatures ≥ 140°C, matching temperatures observed for the Afar (Figures 11–12). The Δ_{47}-temperatures from the majority of depositional carbonates reflect surface temperatures (<40 °C); however, some depositional carbonates from the Sagantole Fm have indications of alteration and reflect association with the As Duma Fault, volcanic centers, and hydrothermal activity. While hydrothermal activity seems to influence the $\delta^{18}O_{carbonate}$ and carbonate Δ_{47}-temperatures, reconstructed $\delta^{18}O_{pw}$ values reflect the isotopic composition of meteoric waters from the Afar today. These reconstructed $\delta^{18}O_{pw}$ values may indicate that hydrothermal fluids are from meteoric water, which is consistent with other studies from rift settings that calculate $\delta^{18}O_{pw}$ values using Δ_{47}-temperatures. Overall, carbonate Δ_{47}-temperatures seem to be a dominant control on the $\delta^{18}O_{carbonate}$ of the carbonates studied in this thesis.

Proximity to volcanism, faults, and indications of hydrothermal activity appears to be the primary control on carbonate Δ_{47} temperatures. The main take-home points from this thesis are 1) carbonates within Pliocene to Pleistocene strata in Afar rift basins can record indications of the elevated temperatures in the Afar; 2) local heat sources (associated with hydrothermal activity, faults, and volcanoes) can alter the isotopic signatures of depositional carbonates, which can affect the isotope-based paleoenvironmental records; and 3) it is possible to screen for the influence of high heat flow on depositional carbonates and use them as valid recorders of paleoenvironmental information when isotopic data are coupled with a combination of field observations, petrographic data, and isotopic data from non-depositional carbonates. The work from this thesis indicates the promise of including Δ_{47} temperature data to study carbonate paragenesis in the Afar.

Acknowledgments

References

Alemayehu, T., Kebede, S., Liu, L. B., and Kebede, T., 2017, Basin hydrogeological characterization using remote sensing, hydrogeochemical and isotope methods (the case of Baro-Akobo, Eastern Nile, Ethiopia): Environmental Earth Sciences, v. 76, no. 13.

Alene, M., Hart, W. K., Saylor, B. Z., Deino, A., Mertzman, S., Haile-Selassie, Y., and Gibert, L. B., 2017, Geochemistry of Woranso-Mille Pliocene basalts from west-central Afar, Ethiopia: Implications for mantle source characteristics and rift evolution: Lithos, v. 282, p. 187-200.

Aronson, J. L., Hailemichael, M., and Savin, S. M., 2008, Hominid environments at Hadar from paleosol studies in a framework of Ethiopian climate change: Journal of Human Evolution, v. 55, no. 4, p. 532-550.

Bedaso, Z. K., DeLuca, N. M., Levin, N. E., Zaitchik, B. F., Waugh, D. W., Wu, S. Y., Harman, C. J., and Shanko, D., 2020, Spatial and temporal variation in the isotopic composition of Ethiopian precipitation: Journal of Hydrology, v. 585.

Bedaso ZK, Levin NE, Passey BH, Quade J, Semaw S, Rogers MJ, Saylor BZ, Haile-Selassie Y. Consistently hot Afar soils since the Pliocene: evidence from paleosol carbonate clumped isotope paleothermometry. In preparation for Geology.

Bekele, Berhanu., 2012. Geological Survey of Ethiopia Geothermal Resource Exploration and Evaluation Directorate: Review and Reinterpretation of Geophysical Data of Tendaho Geothermal Field: Geological Survey of Ethiopia.

Bekele, T. G., Ambelu, A., Chegen, R. G., Bekele, A. G., Mekonen, S., and Endale, H., 2021, Relevance of macroinvertebrate communities as a water quality monitoring tool in ecosystems under harsh environmental conditions in the Rift Valley region: Environmental Monitoring and Assessment, v. 193, no. 3.

Bergman, S. C., Huntington, K. W., and Crider, J. G., 2013, Tracing paleofluid sources using clumped isotope thermometry of diagenetic cements along the Moab Fault, Utah: American Journal of Science, v. 313, no. 5, p. 490.

Beverly, E. J., Levin, N. E., Passey, B. H., Aron, P. G., Yarian, D. A., Page, M., and Pelletier, E. M., 2021, Triple oxygen and clumped isotopes in modern soil carbonate along an aridity gradient in the Serengeti, Tanzania: Earth and Planetary Science Letters, v. 567, p. 116952.

Beyene, A., and Abdelsalam, M. G., 2005, Tectonics of the Afar Depression: A review and synthesis: Journal of African Earth Sciences, v. 41, no. 1, p. 41-59.

Blomgren, V. J., Crossey, L. J., Karlstrom, K. E., Fischer, T. P., and Darrah, T. H., 2019, Hot spring hydrochemistry of the Rio Grande rift in northern New Mexico reveals a distal geochemical connection between Valles Caldera and Ojo Caliente: Journal of Volcanology and Geothermal Research, v. 387, p. 106663.

Bonifacie, M., Calmels, D., Eiler, J. M., Horita, J., Chaduteau, C., Vasconcelos, C., Agrinier, P., Katz, A., Passey, B. H., Ferry, J. M., and Bourrand, J.-J., 2017, Calibration of the dolomite clumped isotope thermometer from 25 to 350°C, and implications for a universal calibration for all (Ca, Mg, Fe) CO_3 carbonates: Geochimica et Cosmochimica Acta, v. 200, p. 255-279.

Brenner, D. C., Passey, B. H., Holder, R. M., and Viete, D. R., 2021, Clumped-Isotope Geothermometry and Carbonate U–Pb Geochronology of the Alta Stock Metamorphic Aureole, Utah, USA: Insights on the Kinetics of Metamorphism in Carbonates: Geochemistry, Geophysics, Geosystems, v. 22, no. 4.

Brigaud, B., Bonifacie, M., Pagel, M., Blaise, T., Calmels, D., Haurine, F., and Landrein, P., 2020, Past hot fluid flows in limestones detected by Δ_{47}-(U-Pb) and not recorded by other geothermometers: Geology, v. 48, no. 9, p. 851-856.

Cavalazzi, B., Barbieri, R., Gomez, F., Capaccioni, B., Olsson-Francis, K., Pondrelli, M., Rossi, A. P., Hickman-Lewis, K., Agangi, A., Gasparotto, G., Glamoclija, M., Ori, G. G., Rodriguez, N., and Hagos, M., 2019, The Dallol Geothermal Area, Northern Afar (Ethiopia)-An Exceptional Planetary Field Analog on Earth: Astrobiology, v. 19, no. 4, p. 553-578.

Cerling, T. E., 1992, Development of grasslands and savannas in East Africa during the Neogene: Palaeogeography, Palaeoclimatology, Palaeoecology, v. 97, no. 3, p. 241-247.

Chen, S., Ryb, U., Piasecki, A. M., Lloyd, M. K., Baker, M. B., and Eiler, J. M., 2019, Mechanism of solid-state clumped isotope reordering in carbonate minerals from aragonite heating experiments: Geochimica Et Cosmochimica Acta, v. 258, p. 156-173.

Chorowicz, J., 2005, The East African rift system: Journal of African Earth Sciences, v. 43, no. 1-3, p. 379-410.

Deino, A. L., Scott, G. R., Saylor, B., Alene, M., Angelini, J. D., and Haile-Selassie, Y., 2010, [40]Ar/[39]Ar dating, paleomagnetism, and tephrochemistry of Pliocene strata of the hominid-bearing Woranso-Mille area, west-central Afar Rift, Ethiopia: Journal of Human Evolution, v. 58, no. 2, p. 111-126.

deMenocal, P. B., 2004, African climate change and faunal evolution during the Pliocene–Pleistocene: Earth and Planetary Science Letters, v. 220, no. 1, p. 3-24.

Eiler, J. M., 2007, "Clumped-isotope" geochemistry—The study of naturally-occurring, multiply-substituted isotopologues: Earth and Planetary Science Letters, v. 262, no. 3, p. 309-327.

Ghosh, P., Adkins, J., Affek, H., Balta, B., Guo, W., Schauble, E. A., Schrag, D., and Eiler, J. M., 2006, [13]C–[18]O bonds in carbonate minerals: A new kind of paleothermometer: Geochimica et Cosmochimica Acta, v. 70, no. 6, p. 1439-1456.

Gizaw, B., 1996, The origin of high bicarbonate and fluoride concentrations in waters of the Main Ethiopian Rift Valley, East African Rift system: Journal of African Earth Sciences, v. 22, no. 4, p. 391-402.

Haile-Selassie, Y., Deino, A., Saylor, B., Umer, M., and Latimer, B., 2007, Preliminary geology and paleontology of new hominid-bearing Pliocene localities in the central Afar region of Ethiopia: Anthropological Science, v. 115, no. 3, p. 215-222.

Haile-Selassie, Y., Melillo, S. M., Ryan, T. M., Levin, N. E., Saylor, B. Z., Deino, A., Mundil, R., Scott, G., Alene, M., and Gibert, L., 2016, Dentognathic remains of Australopithecus afarensis from Nefuraytu (Woranso-Mille, Ethiopia): Comparative description, geology, and paleoecological context: Journal of Human Evolution, v. 100, p. 35-53.

Henkes, G. A., Passey, B. H., Grossman, E. L., Shenton, B. J., Perez-Huerta, A., and Yancey, T. E., 2014, Temperature limits for preservation of primary calcite clumped isotope paleotemperatures: Geochimica et Cosmochimica Acta, v. 139, p. 362-382.

Henkes, G. A., Passey, B. H., Wanamaker, A. D., Grossman, E. L., Ambrose, W. G., and Carroll, M. L., 2013, Carbonate clumped isotope compositions of modern marine mollusk and brachiopod shells: Geochimica et Cosmochimica Acta, v. 106, p. 307-325.

Hoareau, G., Crognier, N., Lacroix, B., Aubourg, C., Roberts, N. M. W., Niemi, N., Branellec, M., Beaudoin, N., and Suárez Ruiz, I., 2021, Combination of Δ_{47} and U-Pb dating in tectonic calcite

veins unravel the last pulses related to the Pyrenean Shortening (Spain): Earth and Planetary Science Letters, v. 553, p. 116636.

Hodson, K. R., Crider, J. G., and Huntington, K. W., 2016, Temperature and composition of carbonate cements record early structural control on cementation in a nascent deformation band fault zone: Moab Fault, Utah, USA: Tectonophysics, v. 690, p. 240-252.

Houssein, B., Chandrasekharam, D., Chandrasekhar, V., and Jalludin, M., 2014, Geochemistry of thermal springs around Lake Abhe, Western Djibouti: International Journal of Sustainable Energy, v. 33, no. 6, p. 1090-1102.

Kebede, S., Charles, K., Godfrey, S., MacDonald, A., and Taylor, R. G., 2021, Regional-scale interactions between groundwater and surface water under changing aridity: evidence from the River Awash Basin, Ethiopia: Hydrological Sciences Journal-Journal Des Sciences Hydrologiques, v. 66, no. 3, p. 450-463.

Kele, S., Breitenbach, S. F. M., Capezzuoli, E., Meckler, A. N., Ziegler, M., Millan, I. M., Kluge, T., Deák, J., Hanselmann, K., John, C. M., Yan, H., Liu, Z., and Bernasconi, S. M., 2015, Temperature dependence of oxygen- and clumped isotope fractionation in carbonates: A study of travertines and tufas in the 6–95 °C temperature range: Geochimica et Cosmochimica Acta, v. 168, p. 172-192.

Kelson, J. R., Huntington, K. W., Breecker, D. O., Burgener, L. K., Gallagher, T. M., Hoke, G. D., and Petersen, S. V., 2020, A proxy for all seasons? A synthesis of clumped isotope data from Holocene soil carbonates: Quaternary Science Reviews, v. 234, p. 106259.

Kelson, J. R., Huntington, K. W., Schauer, A. J., Saenger, C., and Lechler, A. R., 2017, Toward a universal carbonate clumped isotope calibration: Diverse synthesis and preparatory methods suggest a single temperature relationship: Geochimica et Cosmochimica Acta, v. 197, p. 104-131.

Lacroix, B., and Niemi, N. A., 2019, Investigating the effect of burial histories on the clumped isotope thermometer: An example from the Green River and Washakie Basins, Wyoming: Geochimica et Cosmochimica Acta, v. 247, p. 40-58.

Levin, N. E., Quade, J., Simpson, S. W., Semaw, S., and Rogers, M., 2004, Isotopic evidence for Plio-Pleistocene environmental change at Gona, Ethiopia: Earth and Planetary Science Letters, v. 219, no. 1-2, p. 93-110.

Levin, N. E., Simpson, S. W., Quade, J., Cerling, T. E., and Frost, S. R., 2008, Herbivore enamel carbon isotopic composition and the environmental context of Ardipithecus at Gona, Ethiopia, in Quade, J., and Wynn, J. G., eds., Geology of Early Humans in the Horn of Africa, Volume 446, p. 215-234.

Levin, N. E., Zipser, E. J., and Cerling, T. E., 2009, Isotopic composition of waters from Ethiopia and Kenya: Insights into moisture sources for eastern Africa: Journal of Geophysical Research-Atmospheres, v. 114.

Lüdecke, T., Kullmer, O., Wacker, U., Sandrock, O., Fiebig, J., Schrenk, F., and Mulch, A., 2018, Dietary versatility of Early Pleistocene hominins: Proceedings of the National Academy of Sciences, v. 115, no. 52, p. 13330-13335.

Luetkemeyer, P. B., Kirschner, D. L., Huntington, K. W., Chester, J. S., Chester, F. M., and Evans, J. P., 2016, Constraints on paleofluid sources using the clumped-isotope thermometry of carbonate veins from the SAFOD (San Andreas Fault Observatory at Depth) borehole: Tectonophysics, v. 690, p. 174-189.

Mangenot, X., Bonifacie, M., Gasparrini, M., Götz, A., Chaduteau, C., Ader, M., and Rouchon, V., 2017, Coupling Δ_{47} and fluid inclusion thermometry on carbonate cements to precisely reconstruct the

temperature, salinity and $\delta^{18}O$ of paleo-groundwater in sedimentary basins: Chemical Geology, v. 472, p. 44-57.

Minissale, A., Corti, G., Tassi, F., Darrah, T. H., Vaselli, O., Montanari, D., Montegrossi, G., Yirgu, G., Selmo, E., and Teclu, A., 2017, Geothermal potential and origin of natural thermal fluids in the northern Lake Abaya area, Main Ethiopian Rift, East Africa: Journal of Volcanology and Geothermal Research, v. 336, p. 1-18.

Passey, B. H., and Ji, H. Y., 2019, Triple oxygen isotope signatures of evaporation in lake waters and carbonates: A case study from the western United States: Earth and Planetary Science Letters, v. 518, p. 1-12.

Passey, B. H., and Levin, N. E., 2021, Triple Oxygen Isotopes in Meteoric Waters, Carbonates, and Biological Apatites: Implications for Continental Paleoclimate Reconstruction, in Bindeman, I. N., and Pack, A., eds., Triple Oxygen Isotope Geochemistry, Volume 86, p. 429-461.

Passey, B. H., Levin, N. E., Cerling, T. E., Brown, F. H., and Eiler, J. M., 2010, High-temperature environments of human evolution in East Africa based on bond ordering in paleosol carbonates: Proceedings of the National Academy of Sciences of the United States of America, v. 107, no. 25, p. 11245-11249.

Petersen, S. V., Defliese, W. F., Saenger, C., Daeron, M., Huntington, K. W., John, C. M., Kelson, J. R., Bernasconi, S. M., Colman, A. S., Kluge, T., Olack, G. A., Schauer, A. J., Bajnai, D., Bonifacie, M., Breitenbach, S. F. M., Fiebig, J., Fernandez, A. B., Henkes, G. A., Hodell, D., Katz, A., Kele, S., Lohmann, K. C., Passey, B. H., Peral, M. Y., Petrizzo, D. A., Rosenheim, B. E., Tripati, A., Venturelli, R., Young, E. D., and Winkelstern, I. Z., 2019, Effects of Improved ^{17}O Correction on Inter-laboratory Agreement in Clumped Isotope Calibrations, Estimates of Mineral-Specific Offsets, and Temperature Dependence of Acid Digestion Fractionation: Geochemistry Geophysics Geosystems, v. 20, no. 7, p. 3495-3519.

Quade, J., Eiler, J., Daëron, M., and Achyuthan, H., 2013, The clumped isotope geothermometer in soil and paleosol carbonate: Geochimica et Cosmochimica Acta, v. 105, p. 92-107.

Quade, J., Levin, N., Semaw, S., Stout, D., Renne, R., Rogers, M., and Simpson, S., 2004, Paleoenvironments of the earliest stone toolmakers, Gona, Ethiopia: Geological Society of America Bulletin, v. 116, no. 11-12, p. 1529-1544.

Quade, J., Levin, N. E., Simpson, S. W., Butler, R., McIntosh, W. C., Semaw, S., Kleinsasser, L., Dupont-Nivet, G., Renne, P., and Dunbar, N., 2008, The geology of Gona, Afar, Ethiopia, in Quade, J., and Wynn, J. G., eds., Geology of Early Humans in the Horn of Africa, Volume 446, p. 1-31.

Renaut, R. W., Jones, B., Tiercelin, J. J., and Tarits, C., 2002, Sublacustrine precipitation of hydrothermal silica in rift lakes: evidence from Lake Baringo, central Kenya Rift Valley: Sedimentary Geology, v. 148, no. 1-2, p. 235-257.

Renaut, R. W., Owen, R. B., Jones, B., Tiercelin, J. J., Tarits, C., Ego, J. K., and Konhauser, K. O., 2013, Impact of lake-level changes on the formation of thermogene travertine in continental rifts: Evidence from Lake Bogoria, Kenya Rift Valley: Sedimentology, v. 60, no. 2, p. 428-468.

Saylor, B. Z., Angelini, J., Deino, A., Alene, M., Fournelle, J. H., and Haile-Selassie, Y., 2016, Tephrostratigraphy of the Waki-Mille area of the Woranso-Mille paleoanthropological research project, Afar, Ethiopia: Journal of Human Evolution, v. 93, p. 25-45.

Saylor, B. Z., Gibert, L., Deino, A., Alene, M., Levin, N. E., Melillo, S. M., Peaple, M. D., Feakins, S. J., Bourel, B., Barboni, D., Novello, A., Sylvestre, F., Mertzman, S. A., and Haile-Selassie, Y.,

2019, Age and context of mid-Pliocene hominin cranium from Woranso-Mille, Ethiopia: Nature, v. 573, no. 7773, p. 220.

Schauble, E. A., Ghosh, P., and Eiler, J. M., 2006, Preferential formation of $^{13}C–^{18}O$ bonds in carbonate minerals, estimated using first-principles lattice dynamics: Geochimica et Cosmochimica Acta, v. 70, no. 10, p. 2510-2529.

Semaw, S., Renne, P., Harris, J. W. K., Feibel, C. S., Bernor, R. L., Fesseha, N., and Mowbray, K., 1997, 2.5-million-year-old stone tools from Gona, Ethiopia: Nature, v. 385, no. 6614, p. 333-336.

Semaw, S., Simpson, S. W., Quade, J., Renne, P. R., Butler, R. F., McIntosh, W. C., Levin, N., Dominguez-Rodrigo, M., and Rogers, M. J., 2005, Early Pliocene hominids from Gona, Ethiopia: Nature, v. 433, no. 7023, p. 301-305.

Shenton, B. J., Grossman, E. L., Passey, B. H., Henkes, G. A., Becker, T. P., Laya, J. C., Perez-Huerta, A., Becker, S. P., and Lawson, M., 2015, Clumped isotope thermometry in deeply buried sedimentary carbonates: The effects of bond reordering and recrystallization: Geological Society of America Bulletin, v. 127, no. 7-8, p. 1036-1051.

Simpson, S. W., Levin, N. E., Quade, J., Rogers, M. J., and Semaw, S., 2019, Ardipithecus ramidus postcrania from the Gona Project area, Afar Regional State, Ethiopia: Journal of Human Evolution, v. 129, p. 1-45.

Simpson, S. W., Quade, J., Kleinsasser, L., Levin, N., MacIntosh, W., Dunbars, N., and Semaw, S., 2007, Late miocene hominid teeth from Gona project area, Ethiopia: American Journal of Physical Anthropology, p. 219-219.

Swanson, E. M., Wernicke, B. P., Eiler, J. M., and Losh, S., 2012, Temperatures and fluids on faults based on carbonate clumped–isotope thermometry: American Journal of Science, v. 312, no. 1, p. 1.

Tierney, J. E., deMenocal, P. B., and Zander, P. D., 2017, A climatic context for the out-of-Africa migration: Geology, v. 45, no. 11, p. 1023-1026.

Wynn, J. G., 2000, Paleosols, stable carbon isotopes, and paleoenvironmental interpretation of Kanapoi, Northern Kenya: Journal of Human Evolution, v. 39, no. 4, p. 411-432.

Zan, L., Gianelli, G., Passerini, P., Troisi, C., and Haga, A. O., 1990, Geothermal exploration in the republic of djibouti: thermal and geological data of the hanlé and asal areas: Geothermics, v. 19, no. 6, p. 561-582.

List of Tables

## List of Figures

Supplementary Material

Supplemental Figure 1: Raw plots of XRD data with data from all samples plotted together. The results from each sample overlap showing the similarities in mineralogy among all the samples. Note WMJQ-006 is not a part of this study.
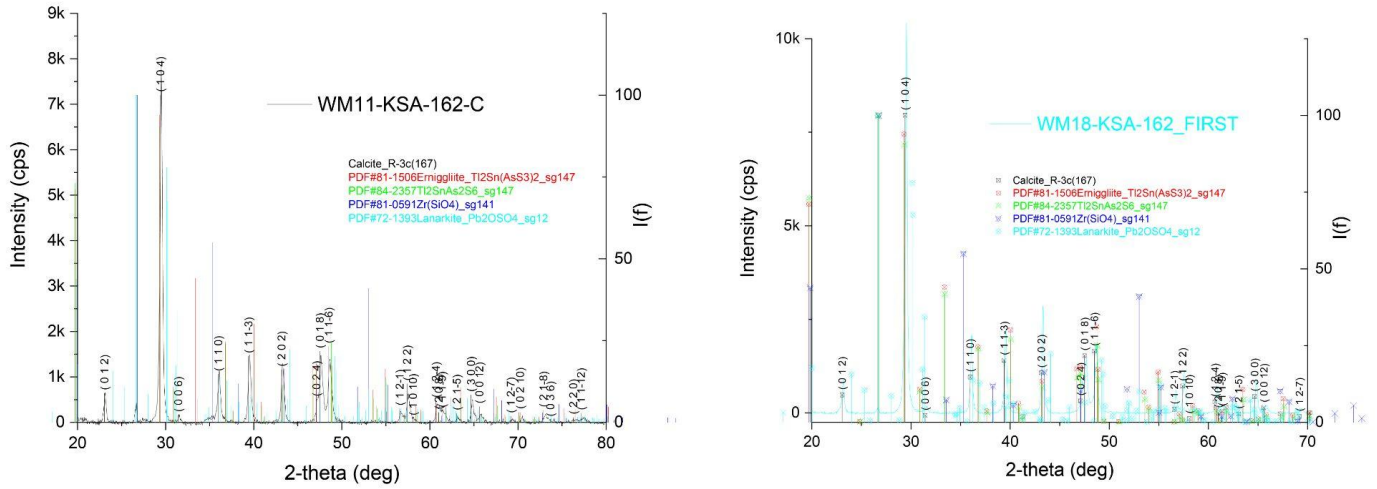
Supplemental Figure 2: Raw XRD data of WM11-KSA-162. The left graph is XRD data of the mineralogy of the core in the radial concretion. The right graph is the mineralogy of the radial fibrous material surrounding the core. Both materials are majority calcite.
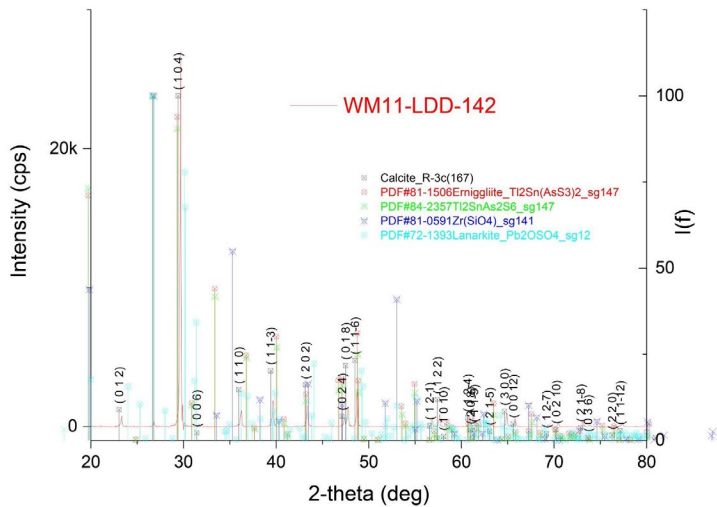
Supplemental Figure 3: Raw XRD data of WM11-LDD-142 Radial fibrous material. The radial concretion is majority calcite.
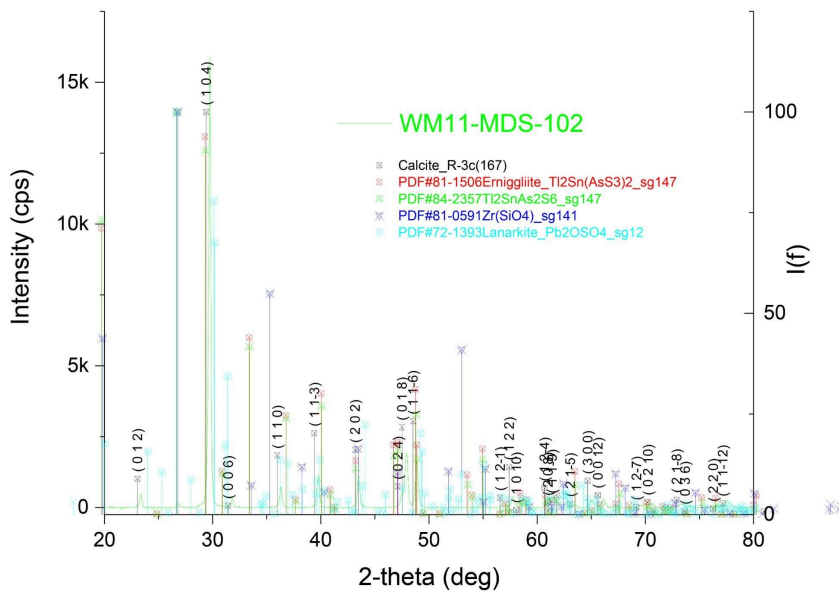
Supplemental Figure 4: Raw XRD data of WM11-MSD-102. The fault carbonate is majority calcite.